JOURNAL OF COMPUTATIONAL PHYSICS 106, 234–257 (1993)

Chebyshev Collocation Method and Multi-domain Decomposition for Navier–Stokes Equations in Complex Curved Geometries

C. R. SCHNEIDESCH AND M. O. DEVILLE

Université Catholique de Louvain, Unité de Mécanique Appliquée, Louvain-La-Neuve, Belgium

Received July 19, 1991

A general multidomain decomposition is proposed for the numerical solution of the 2D incompressible stationary Navier–Stokes equations. The solution technique consists in a Chebyshev orthogonal collocation method preconditioned by a standard Galerkin finite element technique. The preconditioned system is then solved through a Richardson procedure. The domain of interest is decomposed into quadrilaterals, curved when needed. A Gordon transfinite interpolation performs the curvilinear grid generation of the obtained simply-connected planar subdomains. The interface conditions, naturally incorporated into the finite element approach, relate neighbour subdomains through the normal jump of appropriate fluxes across internal boundaries, where an integral form of C^1 continuity is consequently achieved at convergence of the iterative processes. The study of model Stokes problems demonstrates that the current method still behaves spectrally in distorted geometries. For curvilinear distortion, a loss of several orders of magnitude is observed in the solution accuracy even when the distortion is very limited. Finally, some results of flow simulation in a constricted channel are proposed to illustrate the abilities of the present method to treat Navier–Stokes problems.

1. INTRODUCTION

Various spectral methods are currently developed and used in computational fluid dynamics. Their major advantage is the high accuracy attained by the resulting discretization for a given number of nodes or, consequently, the saving of the computational ressources for a given accuracy. The difficulty to apply such methods to real-life problems arises when the geometry to be considered departs from a simple rectangle, as first emphasized by Orszag [29].

In the past decade intensive research has been devoted to overcome this apparent limitation. The present cure techniques may be set into two main categories, although combinations of both are effectively used. On the one hand, domain decomposition methods allow the partitioning of the global geometry into elementary quadrangles. Active investigation still goes on in this field, as underlined by the numerous contributions to dedicated symposiums [5, 6]. On the other hand, suitable coordinate transformations are created in order to map the arbitrary physical domain into the reference square space where the polynomial basis used as interpolants are defined. For 2D computations, such transformation methods take on different forms: algebraic interpolation, conformal mapping, or the solution of differential equations, summing up in a widespread field as surveyed, for instance, by Eiseman [17]. Some spectral practitioners proposed their own technique to cope with non-rectangular geometries. In the case of the numerical solution of the Navier–Stokes equations, Patera and coworkers [26] developed the spectral element method which combines mappings to a domain decomposition strategy [25]. Curvilinear subdomains were incorporated by Metivet [27] into a Schwarz domain decomposition algorithm applied to a spectral collocation method.

In the same framework of spectral methods for curved geometries, we propose a preconditioned Chebyshev collocation technique [13] to solve the 2D incompressible stationary Navier–Stokes equations in the primitive variables formulation. The dependent variables are represented by a series of basis functions involving Chebyshev polynomials. A Newton linearization is carried out on the continuous equations. The problem discretization is then achieved by an orthogonal collocation method. To improve the conditioning of the resulting system of algebraic equations, this approach is preconditioned by a standard Galerkin finite element (FE) technique, which incorporates the classical nine-node Lagrangian element. The preconditioning then leads us to solve the system through a Richardson iterative procedure. This method presents major numerical advantages [14, 15] and is demonstrated to be an efficient way to attain the attractive properties of a spectral method [9]. Navier–Stokes problems in nontrivial geometries were handled so far through a domain decomposition into rectangular subdomains [10].

In this paper, the method is extended to the solution of

0021-9991/93 $5.00

the governing equations in general complex geometries. The computational domain is decomposed into quadrangles, curved when needed. A Gordon transfinite interpolation [20] performs the curvilinear grid generation of the obtained simply-connected planar subdomains. The mapping is expressed in terms of the parametric representation of the curved boundaries. The resulting collocation grid used to solve the governing equations is parametrizable by polynomials of the same order as the discretization within each considered subdomain. The interface conditions, naturally incorporated into the finite element approach, relate neighbour subdomains through the normal jump of appropriate fluxes across internal boundaries, where an integral form of C^1 continuity is consequently achieved over the velocity field once the iterative procedures have converged.

In the comparison of collocation with other spectral methods, we will refer only to the spectral element method [26] which is significantly different by its underlying principles. In our collocation method, the second-order partial differential equation (pde) is satisfied at given points by the approximate solution. The solution must then belong to a space of functions $H^2(\Omega)$ in which the derivatives of the functions up to the second-order must be square integrable. Even in our technique which is preconditioned by an operator defined from a weak form of the initial problem, the strong formulation of the residuals to the pde must be computed and the functions considered *have* to belong to $H^2(\Omega)$. Conversely, the spectral element method relies on a variational statement of the initial problem. The computation of the variational form involves integration by parts. For second-order pde's, the resulting expression does not contain any second-order derivatives. Thus, such a formulation will be well defined if the first derivative of the solution, rather than the second, is required to be square integrable. Therefore, the possibility arises of enlarging the class of functions which are admissible in the variational problem to a space $H^1(\Omega)$ bigger than $H^2(\Omega)$. Regarding domain decomposition, the flux continuity at element interfaces is automatically satisfied as part of the numerical process of the spectral element method. Because of its variational formulation basis, the method uses trial functions which are C^0 across boundaries. A weak matching of the first derivatives is obtained without the need to impose it explicitly, as the solution is sought in $H^1(\Omega)$. This gives the spectral element method a great deal of flexibility with respect to domain partitioning. Conversely, our technique, derived from strong collocation, requires the enforcement of the continuity of the function *and* of its derivative along each internal boundary created by domain decomposition. We impose, in effect, that the solution *is* C^1. The introduction of the FE preconditioner facilitates somewhat the treatment of the internal boundaries. A more detailed comparison can be found in [30].

Section 2 gives the basic equations. In Section 3, the mathematical tools are defined. The transformation method is presented in Section 4. Section 5 describes briefly the collocation technique and the preconditioned iterative approach. In Section 6, the domain decomposition applied to curved geometries is studied. Section 7 is devoted to the detailed discussion of simulation results of model Stokes problems in complex geometries together with complicated Navier–Stokes flow solutions.

2. BASIC EQUATIONS

The steady-state Navier–Stokes equations are written in stress formulation:

$$\rho(\mathbf{u}\cdot\nabla)\mathbf{u} = \operatorname{div}\boldsymbol{\sigma} + \rho\mathbf{b}, \tag{2.1a}$$

$$\operatorname{div}\mathbf{u} = 0, \tag{2.1b}$$

with the constitutive equations of a newtonian fluid

$$\boldsymbol{\sigma} = -p\mathbf{I} + 2\mu\mathbf{d}, \tag{2.1c}$$

$$\mathbf{d} = \tfrac{1}{2}[\nabla\mathbf{u} + (\nabla\mathbf{u})^{\mathrm{T}}], \tag{2.1d}$$

where $\mathbf{u}$ denotes the velocity field, p the pressure, μ the dynamic viscosity, $\mathbf{b}$ the body force, $\boldsymbol{\sigma}$ the stress tensor, $\mathbf{I}$ the unit tensor, $\mathbf{d}$ the rate of deformation tensor. Each term with the superscript T is transposed. Equation (2.1a) is the momentum equation while Eq. (2.1b) enforces the continuity constraint for incompressible fluids.

Equations (2.1) are solved on the physical domain Ω. The boundary conditions are given by the relationship

$$B\mathbf{u} = \mathbf{g}, \qquad \text{on } \partial\Omega, \tag{2.2}$$

where $\partial\Omega$ represents the external boundary of the domain Ω. If the set Γ contains B boundary segments closing Ω and denoted by Γ^b, $b = 1, ..., B$, the boundary $\partial\Omega$ is thus represented by elements from two subsets of Γ, Γ_e and Γ_n, depending on the type of boundary condition applied on them. At each point of $\partial\Omega$ denoted by its position vector $\mathbf{x}$, we have

essential (Dirichlet) boundary conditions, which apply on each point of $\partial\Omega_e$ composed by elements of Γ_e:

$$\mathbf{u}(\mathbf{x}) = \mathbf{g}_1(\mathbf{x}), \qquad \forall\mathbf{x}\in\partial\Omega_e, \tag{2.3}$$

natural boundary conditions applied on $\partial\Omega_n$ described by elements of $\Gamma_n = \Gamma\backslash\Gamma_e$:

$$\mathbf{t}(\mathbf{x}) = \mathbf{n}\cdot\boldsymbol{\sigma} = \mathbf{g}_2(\mathbf{x}), \qquad \forall\mathbf{x}\in\partial\Omega_n. \tag{2.4}$$

In (2.4), $\mathbf{t}$ is the stress vector which is related to the stress

tensor $\boldsymbol{\sigma}$ through the Cauchy principle (first equality in (2.4)). Here, $\mathbf{n}$ is the unit outward normal vector to $\partial\Omega_n$.

We treat the non-linearity of Eq. (2.1a) by Newton's linearization. Assuming that the Fréchet derivatives of the Navier–Stokes operator exist and denoting by $\delta\mathbf{u}$ and $\delta\boldsymbol{\sigma}$ the variations of the velocity field and the stress tensor, respectively, the linearized Navier–Stokes equations are

$$\rho[(\mathbf{u}^n \cdot \nabla)\,\delta\mathbf{u} + (\delta\mathbf{u} \cdot \nabla)\,\mathbf{u}^n] - \operatorname{div}\delta\boldsymbol{\sigma} = \operatorname{div}\boldsymbol{\sigma}^n + \rho\mathbf{b}^n - \rho(\mathbf{u}^n \cdot \nabla)\,\mathbf{u}^n, \tag{2.5a}$$

$$\operatorname{div}\delta\mathbf{u} = -\operatorname{div}\mathbf{u}^n, \tag{2.5b}$$

for

$$\mathbf{u}^{n+1} = \mathbf{u}^n + \delta\mathbf{u}, \qquad \boldsymbol{\sigma}^{n+1} = \boldsymbol{\sigma}^n + \delta\boldsymbol{\sigma},$$

where the superscript refers to the iteration index of the Newton's scheme. Equations (2.5) are solved with the following boundary conditions:

$$\delta\mathbf{u} = 0, \qquad \forall \mathbf{x} \in \partial\Omega_e, \tag{2.6}$$

and

$$\delta\mathbf{t} = \mathbf{n} \cdot \delta\boldsymbol{\sigma} = -\mathbf{t}^n + \mathbf{g}_2(\mathbf{x}), \qquad \forall \mathbf{x} \in \partial\Omega_n. \tag{2.7}$$

3. NOTATIONS AND DEFINITIONS

Although in this paper the same notations as in [9, 10] are used, they are generalized to the case where a curvilinear coordinates transformation is implied. We introduce the reference square $\hat{\Omega} =]-1, 1[^2$ and its border $\hat{\Gamma}$, described by a set of four intervals $\bar{I} = [-1, +1]$. The closed reference space will be denoted $\bar{\hat{\Omega}}$. In order to map boundary value problems for the partial differential equation defined on Ω onto the reference square, Ω must be a bounded, simply connected, and non-empty subspace of $\mathbb{R}^2$. As previously mentioned, Γ denotes the set of the boundary segments closing the overall domain. Furthermore, we postulate the following assumptions:

- there exists an open subset $\hat{O}$ in $\mathbb{R}^2$ containing $\bar{\hat{\Omega}}$ and an application $\mathbf{F}: \hat{O} \to \mathbb{R}^2$, $\mathbf{F} \in C^s(\hat{O})$, $s \geqslant 1$, injection on $\hat{\Gamma}$. The transformation jacobian $J_{\mathbf{F}}$, for two strictly positive constants α and β, must verify that

$$\forall \mathbf{r} \in \bar{\hat{\Omega}}, \qquad \alpha \leqslant J_{\mathbf{F}}(\mathbf{r}) \leqslant \beta, \tag{3.1}$$

- the application $\mathbf{F}$ maps the reference border $\hat{\Gamma}$ onto the physical domain border Γ:

$$\mathbf{F}(\hat{\Gamma}) = \Gamma. \tag{3.2}$$

The function $\mathbf{F}$ is a continuous vector-valued function of two independent variables. If the function $\mathbf{F}$ satisfies these properties, $\mathbf{F}$ is also a bijection on $\bar{\hat{\Omega}}$ and one may introduce its inverse $\mathbf{F}^{-1} = \mathbf{G}: \bar{\Omega} \to \bar{\hat{\Omega}}$, $\mathbf{G} \in C^0(\bar{\Omega})$. Consequently, we will denote by $\mathbf{r} = \{r, s\}$ any point in $\bar{\hat{\Omega}}$ and by $\mathbf{x} = \{x, y\}$ any point in $\bar{\Omega}$, such that

$$\bar{\Omega} = \{\mathbf{x} = \mathbf{F}(\mathbf{r});\ |r| \leqslant 1,\ |s| \leqslant 1\}. \tag{3.3}$$

The continuous vector-valued diffeomorphism $\mathbf{F}$ of the two independent variables $\{r, s\}$ is of course unknown and we have to construct a univalent function which matches $\mathbf{F}$ on the boundary, in other words create its approximation that we will denote by $\mathbf{F}_{\lambda,\mu}$. For a given space of polynomials $\mathbb{P}_{\lambda,\mu}(\bar{\hat{\Omega}})$ of degree lower or equal to λ (resp. μ) related to the first (resp. second) space coordinate and a projector $I_{\lambda,\mu}: C^0(\bar{\hat{\Omega}}) \to \mathbb{P}_{\lambda,\mu}(\bar{\hat{\Omega}})$, we have

$$\mathbf{F}_{\lambda,\mu} = I_{\lambda,\mu}(\mathbf{F}). \tag{3.4}$$

The discussion of the projector $I_{\lambda,\mu}$ and its consequent approximation $\mathbf{F}_{\lambda,\mu}$ is deferred to a further section. Without going into the details, the discrete mapping $\mathbf{F}_{\lambda,\mu}$ satisfies, by construction, the same assumptions (3.1) to (3.3) as the continuous mapping $\mathbf{F}$.

Let us denote by N the couple $(N_{x_1}, N_{x_2}) \in \mathbb{N} \times \mathbb{N}$, where $\mathbb{N}$ is the set of natural numbers. Spatial discretization proceeds by covering the physical domain $\bar{\Omega}$ with a discrete Chebyshev mesh $\mathcal{G}_N$ which coincides with the domain at the boundaries. The mesh $\mathcal{G}_N$ results from the discrete mapping in the reference square of the Chebyshev grid $\mathcal{g}_N$, itself a tensor product of the one-dimensional Gauss–Lobatto–Chebyshev (GLC) quadrature grid. Thus, one may write

$$\mathcal{G}_N = \mathbf{F}_{\lambda,\mu}(\mathcal{g}_N), \tag{3.5a}$$

$$\mathcal{g}_N = \bigotimes g_{x_i;N_{x_i}}, \qquad i = 1, 2, \tag{3.5b}$$

with $g_{x_i;N_{x_i}}$ being the roots of the equation

$$(1 - z^2)\,T'_{N_{x_i}} = 0, \qquad z \in [-1, 1], \tag{3.6}$$

where $T'_{N_{x_i}}$ denotes the first-order derivative of the Chebyshev polynomial of the first kind and degree N_{x_i}.

Because of the finite element preconditioning of the Chebyshev collocation scheme, a finite element mesh is defined over the collocation grid. Following Ciarlet [8], $\mathcal{Q}_N$ is the collection of K curvilinear quadrangles whose corner vertices coincide with four neighbouring gridpoints of $\mathcal{G}_N$ such that $\mathcal{Q}_N = \bigcup_k Q_k$, $k = 1, ..., K$. Let $\mathbb{P}_{(n,n)}$ denote the space of two-dimensional Lagrangian finite elements which restrict to nth degree interpolants over each quadrangle $Q_k \in \mathcal{Q}_N$. Here, we will restrict ourselves to $n = 1, 2$. The

space $\mathbb{P}_N$ will contain all the continous functions in $\bar{\Omega}$, which are polynomials of degree N_{x_i} in the x_i variable.

The FE spaces are defined in Demaret and Deville [10]. They correspond to the well-known nine-nodes Lagrangian element, where the velocities and pressures are approximated by biquadratic and bilinear interpolants, respectively. In this context, the velocities are searched in $V^0_{2,h}$, the FE discrete space of functions which satisfy homogeneous conditions. The FE and the spectral interpolators, denoted I_h and I_N, respectively, are also introduced in the same paper.

On any point of $\partial\Omega_n$, normal stresses are computed by the spectral interpolation operator $I_{\Gamma,N}$ defined as follows:

$$I_{\Gamma,N} = \begin{cases} \forall \Gamma^b \in \Gamma, \quad b = 1, \ldots, B \\ I_{\Gamma,N}: C^0(\bar{\Gamma}^b) \to \mathbb{P}_{N_{x_i}}, \\ \quad \text{with } N_{x_i} \text{ polynomial degree on } \Gamma^b \\ (I_{\Gamma,N}\mathbf{t})(\mathbf{x}_i) = \mathbf{t}(\mathbf{x}_i), \quad \forall \mathbf{x}_i \in \mathcal{G}_N \cap \Gamma_n \\ 0, \quad \forall \mathbf{x}_i \in \mathcal{G}_N \cap \Gamma_e \end{cases} \tag{3.7}$$

The same operator is applied to the natural boundary condition $\mathbf{g}_2(\mathbf{x}_i)$.

Finally, two other geometric transformations take place in the definition of the problem. We will refer to Fig. 3.1 for these definitions. The first one concerns the local mappings $\mathbf{f}_k^{\text{Phys}}$ from the $[-1, +1] \times [-1, +1]$ parent element ω of the FE technique to the elements of the physical mesh. There exists one of such mappings for any one of the elements. That continuous mapping must satisfy the same properties as the global mapping $\mathbf{F}$. Any point in ω is denoted by its coordinates $\xi = \{\xi, \eta\}$. Let us consider the element $Q_k = \mathcal{Q}_N$ whose vertices belong to the set $\mathcal{G}_{2,N}$ of global nodes for the FE mesh. The element Q_k can be considered as

$$Q_k = \{\mathbf{x} = \mathbf{f}_k^{\text{Phys}}(\xi); |\xi| \leqslant 1, |\eta| \leqslant 1\}. \tag{3.8}$$

The second family of local mappings $\mathbf{f}_k^{\text{Ref}}$ is also defined over the parent element ω but its domain of application is now

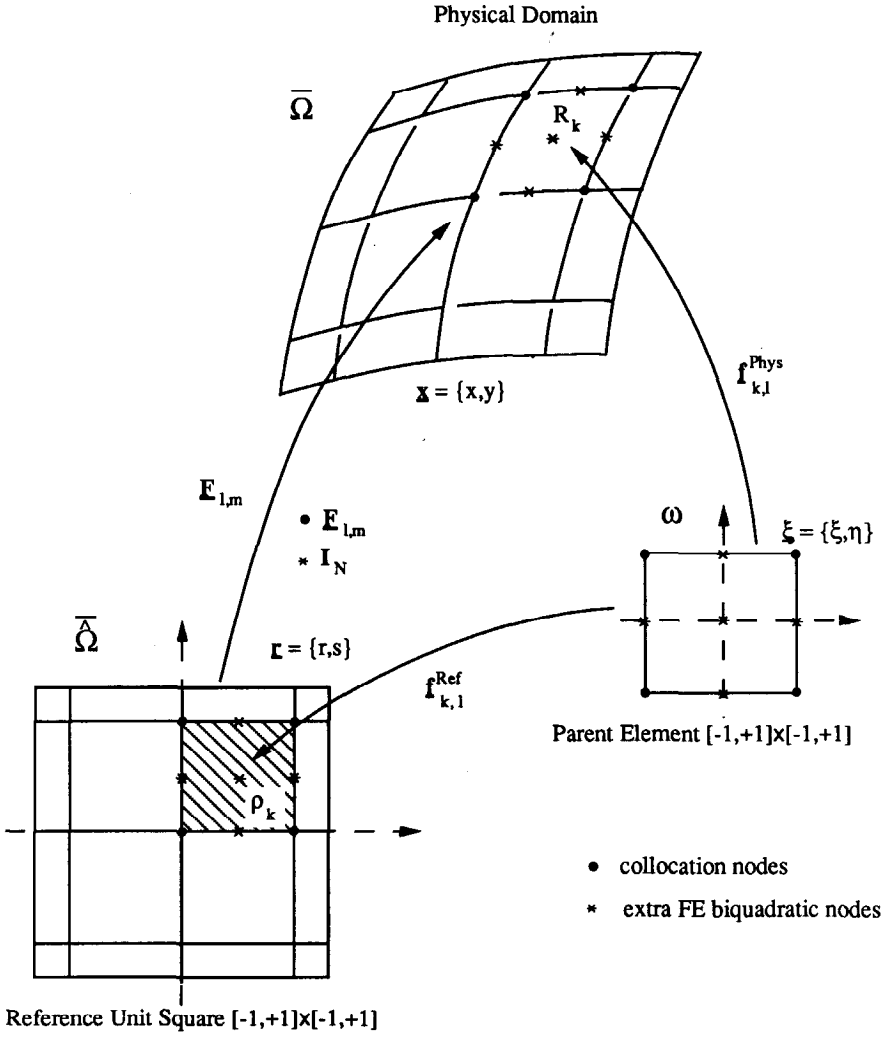

FIG. 3.1. Sketches of the different coordinates transformations involved in the solution procedure.

one of the elements in the reference square. All the nodes in $\mathcal{G}_{2,N}$ supporting the element Q_k are mapped from corresponding nodes in $\mathcal{g}_{2,N}$ through the global vector valued function $\mathbf{F}_{\lambda,\mu}$, the same way as the physical collocation grid $\mathcal{G}_N$ is the mapping of the GLC grid $\mathcal{g}_N$ (Eq. (3.5a)). Thus, it is possible to assess that any element Q_k is the image of one single rectangular element ρ_k of the reference square which is therefore entirely covered by the collection of the ρ_k's.

The element ρ_k in $\bar{\Omega}$ is considered in turn as

$$\rho_k = \{\mathbf{r} = \mathbf{f}_k^{\text{Ref}}(\xi);\ |\xi| \leqslant 1,\ |\eta| \leqslant 1\}, \tag{3.9}$$

and there exists also as many mappings $\mathbf{f}_k^{\text{Ref}}$ as there are elements in the FE mesh.

The continuous functions $\mathbf{f}_k^{\text{Phys}}$ and $\mathbf{f}_k^{\text{Ref}}$ are unknown and approached by suitable approximations $\mathbf{f}_{k,h}^{\text{Phys}}$ and $\mathbf{f}_{k,h}^{\text{Ref}}$, respectively, where h denotes the degree of the interpolation used.

It is important to note that the mappings $\mathbf{f}_k^{\text{Ref}}$ are affine transformations since they map the parent element ω onto rectangles of the GLC grid contrarywise to $\mathbf{f}_k^{\text{Phys}}$ and $\mathbf{F}_{\lambda,\mu}$ which map squares or rectangles onto distorted quadrangles of the physical domain (refer to Fig. 3.1).

All the global and local mappings introduced in this section are of course related. The following conditions must be verified: $\forall \mathbf{x}_\alpha$, $\forall \mathbf{x}_\beta \in Q_k$ in $\bar{\Omega}$, we have

$$\mathbf{x}_\alpha = \mathbf{F}_{\lambda,\mu}(\mathbf{r}_\alpha); \qquad |r| \leqslant 1,\ |s| \leqslant 1, \quad \mathbf{r}_\alpha \in \rho_k, \tag{3.10a}$$

and since $\mathbf{r}_\alpha = \mathbf{f}_{k,h}^{\text{Ref}}(\xi_\alpha)$,

$$\mathbf{x}_\alpha = (\mathbf{F}_{\lambda,\mu} \circ \mathbf{f}_{k,h}^{\text{Ref}})(\xi_\alpha); \qquad |\xi| \leqslant 1,\ |\eta| \leqslant 1, \tag{3.10b}$$

but we have also

$$\mathbf{x}_\beta = \mathbf{f}_{k,h}^{\text{Phys}}(\xi_\alpha); \qquad |\xi| \leqslant 1,\ |\eta| \leqslant 1, \tag{3.10c}$$

and, except for an element of $\mathcal{G}_{2,N}$ (support of the FE isoparametric interpolations $\mathbf{f}_{k,h}^{\text{Phys}}$) a point $\mathbf{x}_\beta$ does not necessarily coincide with the point $\mathbf{x}_\alpha$ for the same ξ_α in the parent element.

4. TRANSFORMATION METHODS

The spatial discretization proceeds by covering the physical non-rectilinear domain with a collocation grid, mapping of a regular Chebyshev grid in $\bar{\Omega}$ (Eqs. (3.5)). The mapping used is an approximation of the continuous unknown mapping.

The key problem is how to create that approximation $\mathbf{F}_{\lambda,\mu}$. That problem was already encountered in finite differences as well as in finite elements and was intensively studied. The methods for 2D structured grid generation are cast into three groups: methods involving the solution of partial differential equations, conformal mappings, and grids created by interpolation from the boundaries. The latter methods were particularly investigated by Gordon *et al.* [20, 21]. Their major advantage is that they can be easily implemented for arbitrary, simply connected, bounded domains. In [18] interpolation from the boundaries compared favorably to different grid generation techniques for the solution of the Poisson equation over non-rectilinear spectral domains. Metivet [27] used the same method in the spectral solution of the Navier–Stokes equations.

Gordon's work postulates the existence of the continuous function $\mathbf{F}$ (a priori unknown) which maps the reference square onto the physical domain (curvilinear quadrangle). The mapping $\mathbf{F}$ satisfies the properties already mentioned in Section 3. Interpolation of $\mathbf{F}$ can be viewed as the search for a projector P such that the projection $P[\mathbf{F}]$, among other interpolation properties, matches $\mathbf{F}$ on the domain boundaries. The projector P is a linear operator whose domain is the linear space $\mathcal{F}$ of continuous functions defined on $\bar{\Omega}$. Given a function $f(z)$: $[-1, +1] \to \mathbb{R}$, Gordon defines its projection $P[f]$ as

$$P[f](z) = \sum_{p=1}^{P} \phi_p(z)\, \lambda_p(f(z)), \tag{4.1}$$

where $\{\lambda_p, p = 1, P\}$ is a set of bounded linear forms over $C^P(\bar{I})$, $\bar{I} = [-1, +1]$ such that, for a point z_p in $\bar{I}$, $\lambda_p(f(z)) = f(z_p)$ and $\{\phi_p, p = 1, P\}$ are the set of orthogonal basis functions in a Lagrange interpolation problem. The two sets satisfy a cardinality relationship:

$$\lambda_l(\phi_p(z)) = \delta_{lp}, \qquad l, p = 1, ..., P, \tag{4.2}$$

with δ_{lp} the Kronecker symbol.

In order to build two-dimensional interpolation, a one-dimensional projector is defined for each coordinate direction in the reference square:

$$P_r[\cdot] = \sum_{p=1}^{P_r} \phi_p^r(r)\, \lambda_p^r(\cdot), \tag{4.3a}$$

$$P_s[\cdot] = \sum_{q=1}^{Q_s} \phi_q^s(s)\, \lambda_q^s(\cdot). \tag{4.3b}$$

The two-dimensional projector $(P_r \oplus P_s)$, defined by the Boolean sum of one-dimensional projectors P_r, P_s, interpolates a function at a non-denumerable set of points as interpolation is performed along the $P_r + Q_s$ lines $r = r_p$, $1 \leqslant p \leqslant P_r$, and $s = s_q$, $1 \leqslant q \leqslant Q_s$. Thus, considering the unknown mapping $\mathbf{F}$, and two interpolation points $(r_1, s_1 = -1, r_2, s_2 = +1)$ in each direction $(P_r, Q_s = 2)$, the projection of $\mathbf{F}$ will involve $\mathbf{F}(r_i, s_j)$, $i, j = 1, 2$, the coordinates in the physical space of the four vertices of the

curvilinear quadrangle and the four parametrizations $\mathbf{F}(r_i, s)$ and $\mathbf{F}(r, s_i)$ which describe the curved side segments.

The mapping of the distorted Chebyshev grid introduced in the previous sections is constructed by means of one of the transformations proposed by Gordon. A linear transfinite interpolation is sufficient to match our only requirement to fit the domain boundaries.

The domain Ω to be discretized is a simply connected open domain, its boundary Γ is a curved quadrilateral, and its vertices are a_i, $1 \leqslant i \leqslant 4$. In addition to the coordinates $\mathbf{a}_i$ of the four vertices, the parametrization $\boldsymbol{\gamma}_i(z)$ of the curves drawing the four curved segments constituting Γ are given.

Each function $\boldsymbol{\gamma}_i: \bar{I} \to \mathbb{R}^2$, $1 \leqslant i \leqslant 4$, must be injective over $\bar{I}$ and verifies the following conditions:

$$\begin{aligned}
&\boldsymbol{\gamma}_1(\bar{I}) \cap \boldsymbol{\gamma}_3(\bar{I}) = \boldsymbol{\gamma}_1(-1) = \boldsymbol{\gamma}_3(-1) = \mathbf{a}_1,\\
&\boldsymbol{\gamma}_2(\bar{I}) \cap \boldsymbol{\gamma}_3(\bar{I}) = \boldsymbol{\gamma}_2(-1) = \boldsymbol{\gamma}_3(+1) = \mathbf{a}_4,\\
&\boldsymbol{\gamma}_2(\bar{I}) \cap \boldsymbol{\gamma}_4(\bar{I}) = \boldsymbol{\gamma}_2(+1) = \boldsymbol{\gamma}_4(+1) = \mathbf{a}_3,\\
&\boldsymbol{\gamma}_1(\bar{I}) \cap \boldsymbol{\gamma}_4(\bar{I}) = \boldsymbol{\gamma}_1(+1) = \boldsymbol{\gamma}_4(-1) = \mathbf{a}_2.
\end{aligned}$$

The boundary Γ is smooth enough to be represented by the $\boldsymbol{\gamma}_i$ functions which are thus assumed to be C^1 over $\bar{I}$. The projector $I_{\lambda,\mu}[\cdot]$ of Eq. (3.4) is identified to the Gordon bilinear projector $(P_r \oplus P_s)[\cdot]$, with $\lambda, \mu = 1$.

The approximate mapping $\mathbf{F}_{1,1}$: $\mathbf{r}_i = \{r, s\} \in \bar{\hat{\Omega}} \to \mathbf{F}_{\lambda,\mu}(\mathbf{r}_i) \in \mathbb{R}^2$ for $\lambda, \mu = 1$ is then

$$\begin{aligned}
\mathbf{F}_{1,1}(r, s) = {} & \phi_1^r(r)\, \boldsymbol{\gamma}_3(s) + \phi_2^r(r)\, \boldsymbol{\gamma}_4(s) + \phi_1^s(s)\, \boldsymbol{\gamma}_1(r)\\
& + \phi_2^s(s)\, \boldsymbol{\gamma}_2(r) - \phi_1^r(r)\, \phi_1^s(s)\, \mathbf{a}_1\\
& - \phi_2^r(r)\, \phi_1^s(s)\, \mathbf{a}_2 - \phi_2^r(r)\, \phi_2^s(s)\, \mathbf{a}_3\\
& - \phi_1^r(r)\, \phi_2^s(s)\, \mathbf{a}_4. \qquad (4.4)
\end{aligned}$$

The so-called blending functions are in this bilinear case for any $r, s \in [-1, 1]$:

$$\phi_1^r(r) = \frac{1-r}{2}, \qquad \phi_2^r(r) = \frac{1+r}{2},$$

$$\phi_1^s(s) = \frac{1-s}{2}, \qquad \phi_2^s(s) = \frac{1+s}{2}.$$

At this stage, it must be emphasized that it is impossible to prove, on a purely analytical or numerical basis, whether or not the approximation $\mathbf{F}_{1,1}(r, s)$ satisfies for any mapping the properties mentioned in Section 3. In order to ensure the correctness of the constructed mapping, those properties are verified over a discrete set of points. The immediate choice in our case is $\mathcal{G}$, the set of all the points $\mathbf{r}_i$ in the reference space such that $\mathbf{F}_{1,1}(\mathbf{r}_i) \in \mathcal{G}_{2,N}$.

For instance, property (3.1) is verified by the existence of two strictly positive constants α' and β' such that

$$\forall \mathbf{r}_i \in \mathcal{G}, \qquad \alpha' \leqslant J_{\mathbf{F}_{1,1}}(\mathbf{r}) \leqslant \beta'. \qquad (4.5)$$

Property (3.2) is of course satisfied by construction of $\mathbf{F}_{1,1}$.

On a purely heuristic basis, the univalency of the mapping is checked graphically. A mapping is accepted if the grid lines of the constructed mesh (i.e., the lines in the physical space images of r = constant or s = constant lines of the reference square) do not intersect anywhere in the physical space.

It remains how to determine the parametrizations $\boldsymbol{\gamma}_i$. We restricted ourselves to the case where the $\boldsymbol{\gamma}_i$ are defined analytically depending on the geometry we want to fit. Generalization to their discrete definition can be considered using basic CAD interpolation tools [28] but will not be discussed here.

Bilinear transfinite interpolation $\mathbf{F}_{1,1}$ together with spectral interpolation generates, therefore, in a pre-processing stage the finite elements meshes $\mathcal{G}_{2,N}$ associated to the collocation grids $\mathcal{G}_N$ which will be used as entry for the Navier–Stokes solver, described in the following sections.

To close this section, we define the approximations of the local auxiliary continuous mappings $\mathbf{f}_k^{\text{Phys}}$ and $\mathbf{f}_k^{\text{Ref}}$ from the parent element ω. The standard approximation in this FE part is isoparametric, and without going into the details, the velocity interpolator defined in Eqs. (3.10) is used for this purpose. We have

$$\mathbf{f}_{k,h}^{\text{Phys}} = I_h \mathbf{f}_k^{\text{Phys}}, \qquad \text{with} \quad h = 2, \qquad (4.6a)$$

$$\mathbf{f}_{k,h}^{\text{Ref}} = I_h \mathbf{f}_k^{\text{Ref}}, \qquad \text{with} \quad h = 2. \qquad (4.6b)$$

5. COLLOCATION METHOD AND FINITE ELEMENT PRECONDITIONING

5.1. *Chebyshev Collocation*

We use orthogonal collocation in the framework of the weighted residual methods [3]. The residuals to the pde's and to the boundary conditions are obtained by inserting finite developments of the dependent variables (velocity, pressure) in terms of basis functions $h_j(z)$ on the reference square $\bar{\hat{\Omega}}$. Denoting by u_N such a dependent variable, one has

$$u_N = \sum_{i=0}^{N_{x_1}} \sum_{j=0}^{N_{x_2}} u_{ij} h_i(r)\, h_j(s) \qquad (5.1)$$

with

$$\begin{aligned}
h_i(z) &= \frac{(1-z^2)\, T'_{N_x}(z)(-1)^{i+1}}{\bar{c}_i N_x^2 (z - z_i)}, \qquad i \in [0, N_x],\\
\bar{c}_0 &= \bar{c}_{N_x} = 2; \qquad \bar{c}_i = 1, \qquad \forall i \in [1, N_x - 1].
\end{aligned} \qquad (5.2)$$

As per the isoparametric interpolation rule, geometry and data are interpolated in the same fashion, that is,

$$x_N = \sum_{i=0}^{N_{x_1}} \sum_{j=0}^{N_{x_2}} x_{ij} h_i(r)\, h_j(s), \tag{5.3a}$$

$$y_N = \sum_{i=0}^{N_{x_1}} \sum_{j=0}^{N_{x_2}} y_{ij} h_i(r)\, h_j(s). \tag{5.3b}$$

The projection method imposes that the scalar product of the residuals with Dirac functions vanishes. Denoting by Res_N these residuals, one obtains

$$(\mathrm{Res}_N(\mathbf{x}_i), \delta(\mathbf{x}-\mathbf{x}_i)) = 0, \qquad \forall \mathbf{x}_i \in \mathscr{G}_N. \tag{5.4}$$

Here, the collocation nodes are those of the physical GLC grid. Applying the collocation procedure to the linearized equations (2.5)–(2.7), the discrete equations in the physical space are expressed as collocation equations over the reference square. Mapping derivation rules gives, in reference square coordinates,

$$\nabla = \frac{1}{J}\left\{\left(-\frac{\partial}{\partial r}\frac{\partial y}{\partial s}+\frac{\partial}{\partial s}\frac{\partial y}{\partial r}\right), \left(\frac{\partial}{\partial r}\frac{\partial x}{\partial s}-\frac{\partial}{\partial s}\frac{\partial x}{\partial r}\right)\right\}, \tag{5.5}$$

with the transformation jacobian J,

$$J = \frac{\partial x}{\partial r}\frac{\partial y}{\partial s}-\frac{\partial y}{\partial r}\frac{\partial x}{\partial s}. \tag{5.6}$$

In order to derive the new discretized equations, we first define the interpolants of the geometric transformation factors,

$$\frac{\partial x_N}{\partial r} = \sum_{i=0}^{N_{x_1}} \sum_{j=0}^{N_{x_2}} x_{ij}^{(r)} h_i(r)\, h_j(s), \tag{5.7a}$$

$$\frac{\partial x_N}{\partial s} = \sum_{i=0}^{N_{x_1}} \sum_{j=0}^{N_{x_2}} x_{ij}^{(s)} h_i(r)\, h_j(s), \tag{5.7b}$$

$$\frac{\partial y_N}{\partial r} = \sum_{i=0}^{N_{x_1}} \sum_{j=0}^{N_{x_2}} y_{ij}^{(r)} h_i(r)\, h_j(s), \tag{5.7c}$$

$$\frac{\partial y_N}{\partial s} = \sum_{i=0}^{N_{x_1}} \sum_{j=0}^{N_{x_2}} y_{ij}^{(s)} h_i(r)\, h_j(s). \tag{5.7d}$$

where the $x_{ij}^{(r)}, \ldots, y_{ij}^{(s)}$ refer to the collocation values of the derivatives in the r or s direction.

The derivation of functions as interpolated by Eq. (5.1) is performed in Chebyshev space as the alternate equivalent form of Eq. (5.1) is

$$u_N = \sum_{n=0}^{N_{x_1}} \sum_{m=0}^{N_{x_2}} \hat{u}_{nm} T_n(r)\, T_m(s), \tag{5.8}$$

because of the peculiar choice of the collocation points. Chebyshev collocation derivation can be accomplished efficiently by the means of a discrete Chebyshev transformation method [13].

Similarly, the discrete mapping jacobian is composed as in Eq. (5.6) through the collocation (physical space) product of the discrete values of expressions (5.7a) to (5.7d) and interpolated by

$$J_N = \sum_{i=0}^{N_{x_1}} \sum_{j=0}^{N_{x_2}} J_{ij} h_i(r)\, h_j(s). \tag{5.9}$$

The discrete equations are formulated in the reference space $\bar{\Omega}$ using the discrete expressions provided by (5.5) through (5.9).

The solution of this resulting algebraic system presents some major drawbacks (discussed in [15]), basically the large bandwidth of the resulting matrix and the $O(N^4)$ conditioning of the viscous part of the operator [22]. Therefore, the collocation system is preconditioned by FE in order to benefit from existing codes with lower computational work [14–16].

5.2. *Finite Element Preconditioning*

The numerical scheme is based on the preconditioned Richardson iteration technique. Formally we write

$$\hat{L}(\delta \mathbf{x}^{k+1} - \delta \mathbf{x}^k) = -\alpha_k (L_C^n \delta \mathbf{x}^k - \mathbf{b}^n), \tag{5.10}$$

where

$$\hat{L} = L_{\mathrm{FE}}$$

is a finite element approximate operator. In (5.10), the superscript k denotes the Richardson index. The initial guess of (5.10) is computed by

$$\delta \mathbf{x}^0 = I_N \mathbf{y}_h, \tag{5.11}$$

where $\mathbf{y}_h$ is the solution of the system resulting from the discretized associated FE problem. A standard Galerkin technique was used for this purpose. More details about this particular part may be found in [10]. The subsequent iterations are carried out using the relationship:

$$\delta \mathbf{x}^{k+1} = \delta \mathbf{x}^k - \alpha_k I_N (L_{\mathrm{FE}}^n)^{-1} \{\mathrm{Res}_{\mathrm{FE}}\}. \tag{5.12}$$

The notation $\mathrm{Res}_{\mathrm{FE}}$ is used for the finite element right-hand side constructed upon the equation residuals when the natural boundary conditions are taken into account. Given a finite element test function $\boldsymbol{\phi}_h$ in $V_{2,h}^0$, we have

$$\mathrm{Res}_{\mathrm{FE}} = \int_\Omega (L_C^n \delta \mathbf{x}^k - \mathbf{b}^n)_N\, \boldsymbol{\phi}_h\, d\Omega + \int_{\partial\Omega_n} (I_{\Gamma,N}(\delta \mathbf{t}^k + \mathbf{t}^n) - I_{\Gamma,N}(\mathbf{g}_2))\, \boldsymbol{\phi}_h\, d\tau. \tag{5.13}$$

The convergence of (5.10) or (5.12) depends strongly on the eigenvalue spectrum of $L_{\mathrm{FE}}^{-1}L_C$. For the Stokes operator over rectangular geometry, Demaret and Deville [9] showed that the nine-nodes Lagrangian element yields an optimum rate of convergence when α_k is set to the value $\frac{2}{3}$. Practically, the same value also produced optimum convergence for Stokes problems over curvilinear geometries.

As the "convergence radius" of the Newton's method is small, the solution for a given Reynolds number is obtained through analytic continuation. The algebraic solver is a sparse matrix Gaussian elimination with minimum degree ordering [19].

6. DOMAIN DECOMPOSITION

The basis for the domain decomposition technique is described in [10]. The domain Ω is broken up into several subdomains Ω^p, $p=1, ..., P$. The decomposition satisfies properties such that in the preconditioner they lead to conforming finite elements over each subdomain.

For each one of those subdomains Ω^p, a suitable mapping associates the GLC grid in the reference square to the corresponding physical collocation grid (or sub-grid) $\mathcal{G}_N^p$. When the geometry departs from the straight rectangle, a Gordon transfinite interpolation from the boundary parametrizations replaces the affine mapping. One has

$$\mathcal{G}_N^p = \mathbf{F}_{\lambda,\mu}^p(\mathcal{G}_N), \tag{6.1}$$

with $\mathcal{G}_N$ defined in (3.5b) and thus $\mathbf{F}_{\lambda,\mu}^p$ either is constructed as in Eq. (4.4) or by simple affine coordinates transformation.

The overall collocation grid is now composed of the collection of the sub-grids $\mathcal{G}_N^p$

$$\mathcal{G}_N = \bigcup_{p=1}^{P} \mathcal{G}_N^p, \tag{6.2}$$

and, similarly, the associated FE mesh is

$$\mathcal{G}_{2,N} = \bigcup_{p=1}^{P} \mathcal{G}_{2,N}^p. \tag{6.3}$$

The space where collocation solutions are sought is defined by

$$\mathbb{P}_N^* = \{v \in C^0(\bar{\Omega}) \mid -v|_{\Omega^p} \in \mathbb{P}_{N^p},\ p=1, ..., P\}, \tag{6.4}$$

where N^p denotes the couple $(N_{x_1}^p, N_{x_2}^p) \in \mathbb{N} \times \mathbb{N}$.

The set Γ contains all the boundary segments in the entire geometry, whether those segments are external or not. The interfaces, i.e., the boundaries of each subdomain Ω^p shared by other subdomains are contained in the subset Γ_i. Therefore, we have

$$\begin{aligned} \Gamma &= \Gamma_e \cup \Gamma_n \cup \Gamma_i, \\ \Gamma_i &= \bigcup_{q=1}^{Q} \Gamma_i^q, \end{aligned} \tag{6.5}$$

with Q as the total number of internal boundary segments appearing in the geometry, independently of any subdomain reference.

The collocation interpolator is extended to the domain decomposition (see [10]). On the set of boundary segments Γ, one defines the spectral interpolation operator:

$$I_{\Gamma,N} = \begin{cases} \forall \Gamma^b \in \Gamma, \quad b=1, ..., B, \\ I_{\Gamma,N}: C^0(\bar{\Gamma}^b) \to \mathbb{P}_{N_{x_j}}, \\ \quad N_{x_j} \text{ polynomial degree on } \Gamma^b, \\ (I_{\Gamma,N}\mathbf{t})(\mathbf{x}_i) = \mathbf{t}(\mathbf{x}_i), \\ \quad \forall \mathbf{x}_i \in \mathcal{G}_N \cap \Gamma_n \text{ and } \mathcal{G}_N \cap \Gamma_i, \\ 0, \quad \forall \mathbf{x}_i \in \mathcal{G}_N \cap \Gamma_e. \end{cases} \tag{6.6}$$

The idea of the interface treatment within the domain decomposition [4] is detailed in [10]. The key lies in the correspondence between an overall solution over the entire domain and the combination of the solutions over each subdomain that one may derive from a weak formulation of the problem. In the decomposed method, each weak solution generates a normal flux (a suitable normal derivative) at the interfaces. When combined to provide the overall solution, those subdomain solutions will be equivalent to the global solution if the interface contributions cancel each other, in other words, if the interface jumps of the normal flux do vanish. If integrated in an iterative process, this is expected to be satisfied at convergence.

In the generalization of this concept to the Navier–Stokes equations, the associated flux is the stress vector (2.4). Consequently, the preconditioned scheme of the linearized Navier–Stokes equations detailed in (5.15) is generalized. We have as before

$$\delta \mathbf{x}^{k+1} = \delta \mathbf{x}^k - \alpha_k I_N (L_{\mathrm{FE}}^n)^{-1} \{\mathrm{Res}_{\mathrm{FE}}\} \tag{6.7}$$

but the term $\mathrm{Res}_{\mathrm{FE}}$ which is the finite element right-hand side constructed upon the equation residuals, takes into account the natural boundary conditions and now incorporates jumps of the normal stress vector. Given a finite element test function $\boldsymbol{\phi}_h$ in $V_{2,h}^0$, we have

$$\begin{aligned} \mathrm{Res}_{\mathrm{FE}} = &\int_\Omega (L_C^n \delta \mathbf{x}^k - \mathbf{b}^n)_N \boldsymbol{\phi}_h \, d\Omega + \int_{\Gamma_n} (I_{\Gamma,N}(\delta \mathbf{t}^k + \mathbf{t}^n) \\ &- I_{\Gamma,N}(\mathbf{g}_2)) \boldsymbol{\phi}_h \, d\tau \\ &- \int_{\Gamma_i} [I_{\Gamma,N}(\delta \mathbf{t}^k + \mathbf{t}^n)] \boldsymbol{\phi}_h \, d\tau, \end{aligned} \tag{6.8}$$

where the term between brackets [ ] indicates the jump of the quantity over one internal boundary segment.

The C^0 continuity of the flux induced at convergence (if any) by a vanishing jump across internal boundaries involves an integral form of C^1 continuity of the velocities over the entire domain and a C^0 continuity of the divergence across internal boundaries.

The computations of the discrete normal flux $\mathbf{t}$ along each segment are performed using Chebyshev interpolants for the components of the Cauchy stress tensor $\boldsymbol{\sigma}$ as well as for the geometric characteristics of the segments (normals $\mathbf{n}$ and the 1D jacobians).

In this last section, a crude estimate of the storage requirements implied by our preconditioned collocation method is presented. We will consider the case of the discretization of the Navier–Stokes equations over one single domain by $\mathcal{N} = N_{x_1} * N_{x_2}$ polynomials. The preconditioned system is the one described in Section 5 which, using FE notations, also takes the form

$$\mathbf{K}\,\delta\mathbf{x} = \mathbf{r}. \tag{6.9}$$

The total number of FE unknowns in the FE preconditioner, by use of $Q2$–$Q1$ FE interpolants, is $\mathcal{NU} = 2 * (2N_{x_1} - 1) * (2N_{x_2} - 1)$ (biquadratic velocity components) $+ \mathcal{N}$ (bilinear pressure), and the number of FE elements is $nelem = (N_{x_1} - 1) * (N_{x_2} - 1)(O(\mathcal{N}))$. The maximum number of connected unknowns in a row of the FE system (6.9) is bounded by 59, as in the FE discretized momentum equations, a velocity unknown on a vertex which belongs to four different elements will be globally connected to $2 * 25$ velocity unknowns and to nine pressure unknowns. In our method, the stiffness matrix $\mathbf{K}$ and the FE r.h.s. $\mathbf{r}$ are built before entering any solution procedure and this requires $59\mathcal{NU}$ (for $\mathbf{K}$) $+ \mathcal{NU}$ (for $\mathbf{r}$) words of storage. The solution is stored in an additional $\mathcal{NU}$ words vector. This evaluation leaves out the extra storage required by the algebraic solver.

7. NUMERICAL RESULTS

In this section, the performances of the method described previously are investigated. When possible, the computed solution is compared to the exact solution through the relative analytical error, denoted by ε_{inf}, evaluated all over the collocation nodes as

$$\varepsilon_{\text{inf}} = \frac{\max_{\mathcal{G}_N}(|\mathbf{x}_{\text{comp}} - \mathbf{x}_{\text{exact}}|)}{\max_{\mathcal{G}_N}(|\mathbf{x}_{\text{exact}}|)}, \tag{7.1}$$

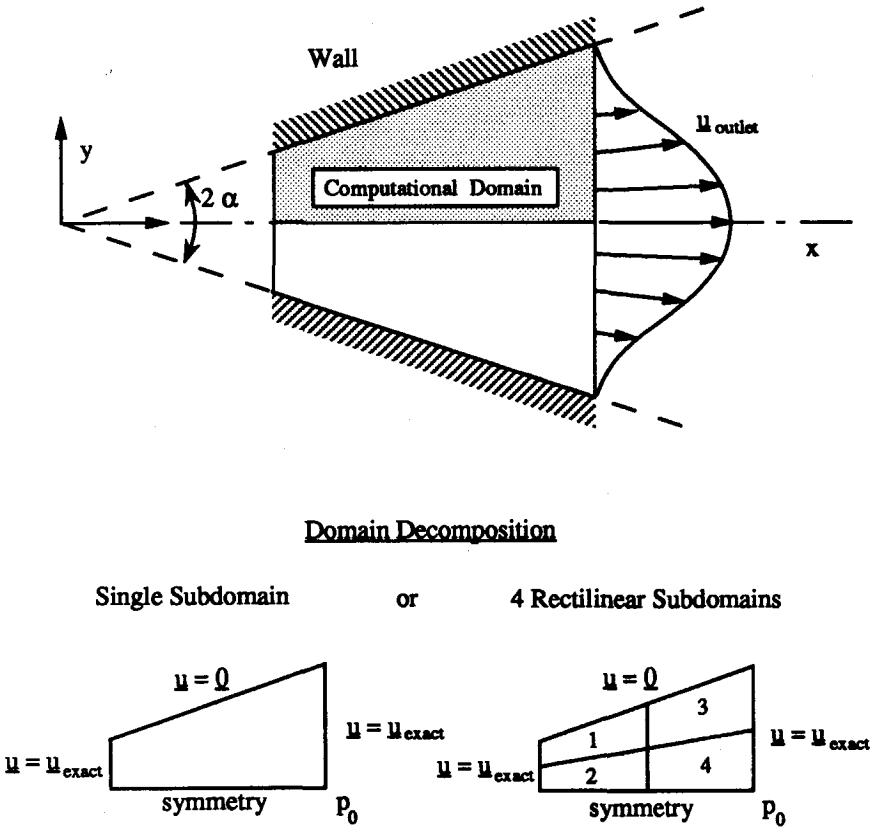

FIG. 7.1. Flow in a divergent channel: problem description and domain decomposition.

where $\mathbf{x}_{exact}$ is the exact solution vector and $\mathbf{x}_{comp}$ the numerical solution. In order to ease the notations, a subdomain is sometimes referred to as a macro (element).

7.1. *Hamel Flow*

To begin with numerical tests, the computed Stokes flow in a divergent channel is compared to the exact solution. The exact solution given by Hamel [23] is written in a 2D Cartesian reference frame as

$$
\begin{aligned}
u &= \frac{\dot{Q}x}{x^2+y^2}\left(\frac{x^2-y^2}{x^2+y^2}-\cos(2\alpha)\right) \\
&\quad \times \frac{1}{\sin(2\alpha)-2\alpha\cos(2\alpha)}, \\
v &= \frac{\dot{Q}y}{x^2+y^2}\left(\frac{x^2-y^2}{x^2+y^2}-\cos(2\alpha)\right) \\
&\quad \times \frac{1}{\sin(2\alpha)-2\alpha\cos(2\alpha)}, \\
p &= \frac{-2\mu\dot{Q}}{x^2+y^2}\frac{x^2-y^2}{x^2+y^2}\frac{1}{\sin(2\alpha)-2\alpha\cos(2\alpha)}+p_0,
\end{aligned}
\tag{7.2}
$$

where $\dot{Q}$ is the flow rate, 2α the total included angle of the aperture, and p_0 is the constant reference pressure.

Figure 7.1 depicts the problem geometry and the type of boundary conditions used in the simulations. The domain is restricted to the upper half of the channel and symmetry is imposed on the axis, while, on the remaining segments, essential boundary conditions are obtained using (7.2). The constant pressure p_0 is determined such as to impose a zero pressure at the tip of the symmetry segment. In all the simulations, the viscosity and the flow rate over the entire divergent were set to 1 and 2, respectively.

This problem was solved for two different apertures ($\alpha = 5$ and $20°$, respectively), using mono-domain as well as multi-domain decomposition. The number of polynomials used is the same in both directions, for all the numerical tests, although this is not constrained by the method. The performances are analyzed as a function of the total number of degrees of freedom (d.o.f.) in both directions regardless of the type of decomposition used. For instance, for 11×11 (global) d.o.f., 11×11 polynomials will generate the spatial discretization of the single domain, whereas the decomposition will use four subdomains discretized by 5×5 polynomials each. Thus, the multi-domain case is said to have 11×11 equivalent (eq.) d.o.f.

7.1.1. *Effect of the rectilinear distortion.* First, we compare solutions produced at 5 and 20° apertures over a single domain. The collocation grid is distorted, although not curved. For both apertures, relative errors (as Eq. (7.1))

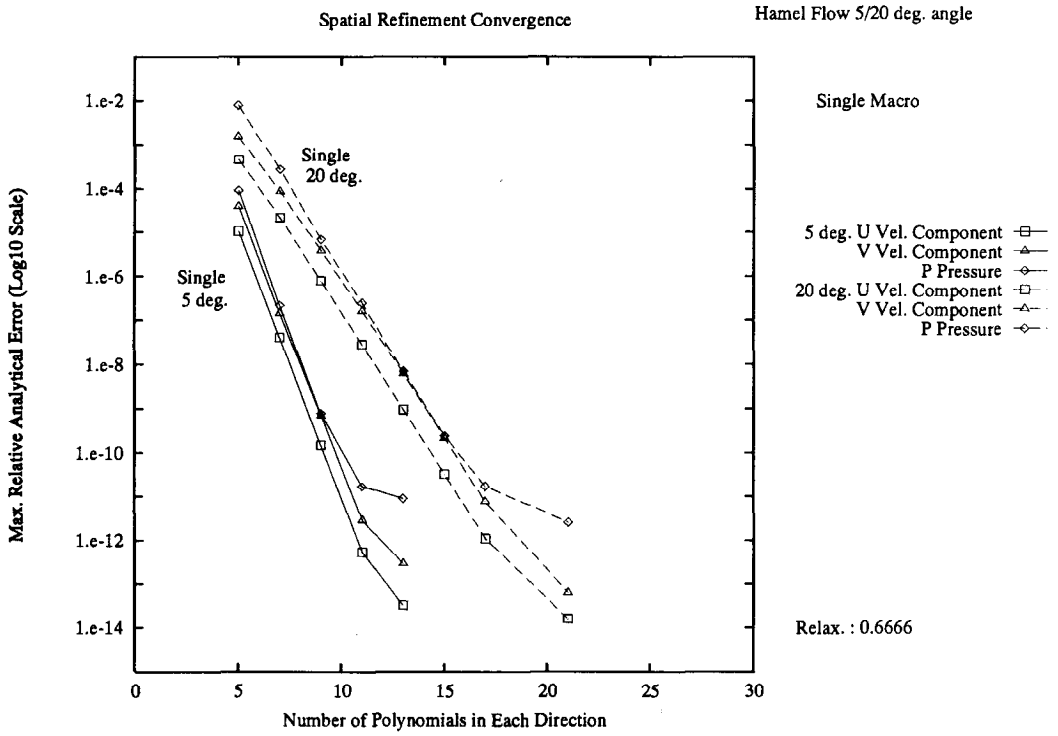

FIG. 7.2. Hamel flow in single domain (5° and 20° angle): spatial refinement convergence. Evolution of the max. relative analytical error (Eq. (7.1)) with respect to the polynomial degree in each direction.

decay exponentially with the increasing global number of degrees of freedom (N). This demonstrates that spectral convergence is achieved by the proposed method. Figure 7.2 compares the spatial refinement effect: the larger included angle and its consequent higher mesh distortion result in a slowed down decay, which remains exponential anyway (globally proportionnal to $e^{-1.7N}$ for a 20° angle against $e^{-2.8N}$ for a 5° angle). One could observe that at equivalent spatial discretization, the consequent accuracy is not as good with a 20°aperture as with a 5° aperture since the solution exhibits more spatial complexity and therefore requires more polynomials to produce an equivalent representation.

The collocation divergence operator may also help to shed light on the effect of the polynomial degree on the achieved accuracy. When applied respectively to the exact and to the computed velocity fields, it informs on how the with the geometric effects, and on how well the computed solution approaches the exact one. Tables I and III report the L_∞ norms (over the collocation nodes) of the collocation divergence operator $\nabla_c \cdot$, applied to the exact and to the converged velocity field as well. This latter case also gives a norm for the strong residual of the continuity equation. All the internal nodes (including interfaces) are involved in the computation of the L_∞ norm. Both values have the same order of magnitude, whatever the spatial discretization is, and drop down to 10^{-12} with increasing polynomial degree.

TABLE I

Hamel Flow 5° Angle, Single Domain

d.o.f.	$\nabla_c \cdot (\mathbf{u}_{exact})$	$\nabla_c \cdot (\mathbf{u}_{comp})$
5 × 5	6.0673e − 05	7.1511e − 05
9 × 9	2.5873e − 10	1.2501e − 09
13 × 13	6.4614e − 13	1.7533e − 12

Note. L_∞ norms of collocation divergence operator ($\nabla_c \cdot$) applied to the exact velocity field ($\mathbf{u}_{exact}$) (Eqs. (7.2)) and the computed one ($\mathbf{u}_{comp}$) for different global number of d.o.f.

This indicates that for a given polynomial degree, the solution obtained at the end of the iterative process could only be improved by increasing the number of polynomials to represent it. In the rectilinear case (5 and 20°), the error due to transformation F is a second-order polynomial and may be represented with full accuracy by very few Chebyshev polynomials.

Convergence histories of the Richardson processes exhibits the same dependency: one reaches a stagnation plateau or goes down to machine accuracy, depending on the number of Chebyshev polynomials used. Typical convergence histories are compared, for instance, in Fig. 7.3 for a 20°-aperture single domain case. When the degree is large enough (21 × 21 polynomials in each direction), 25 itera-

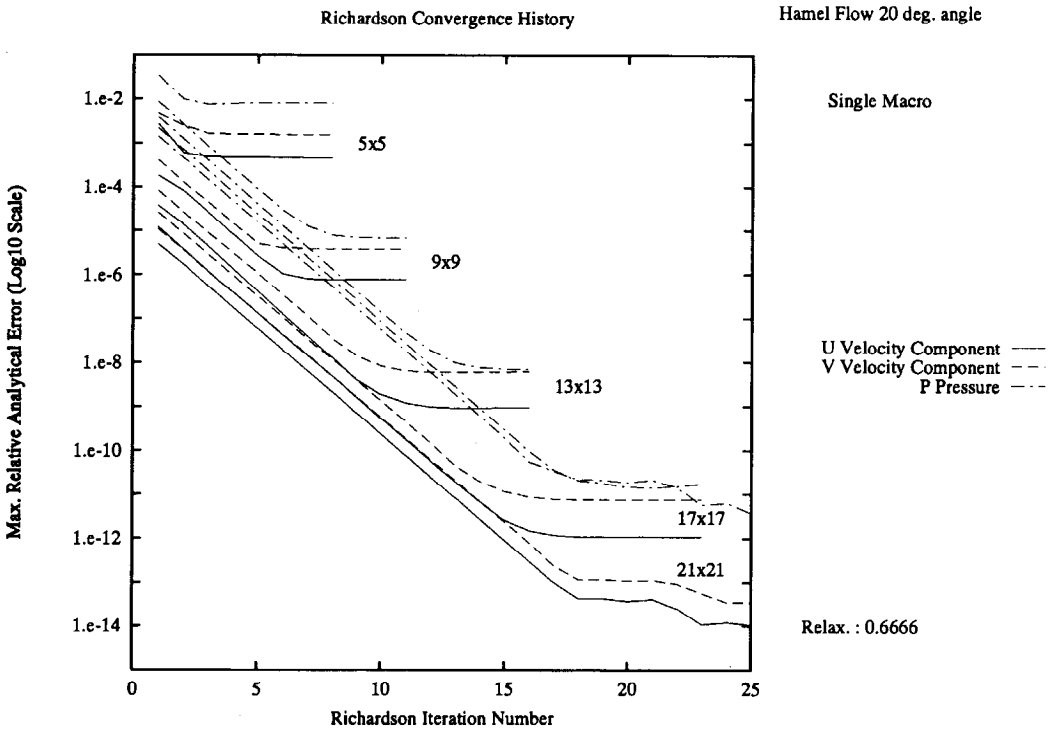

FIG. 7.3. Hamel flow in single domain 20° angle: Richardson convergence history. Evolution of the maximum relative analytical error during the Richardson process with respect to the polynomial degree in each direction.

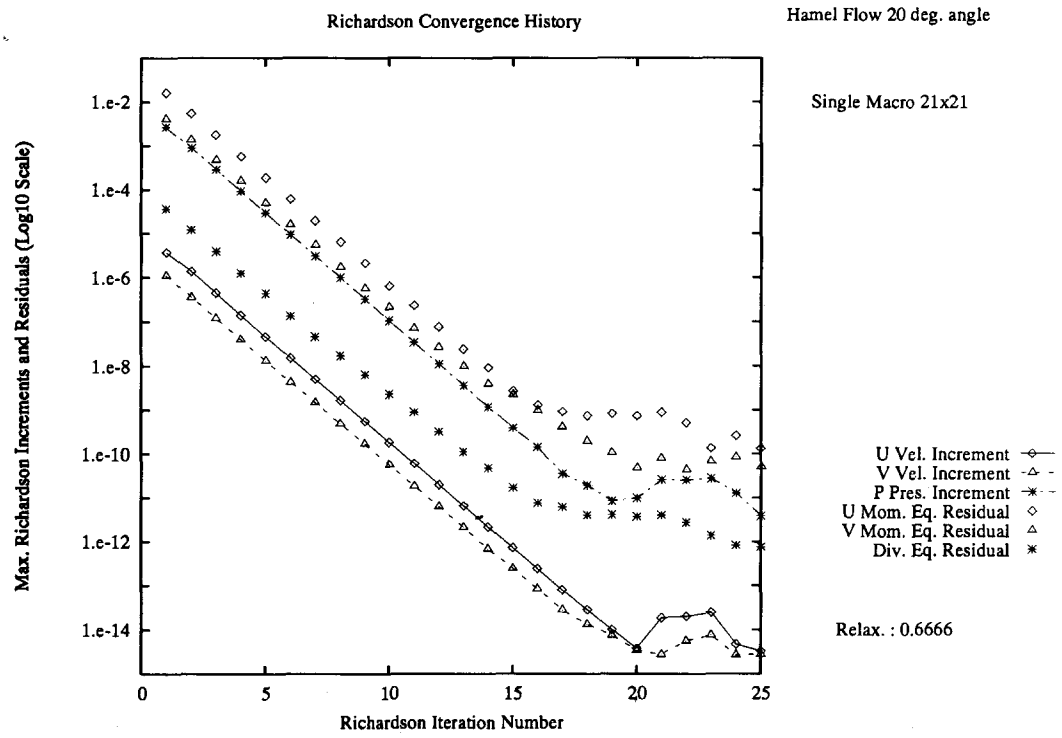

FIG. 7.4. Hamel flow in single domain 20° angle (21 × 21 d.o.f.): Richardson convergence history. Evolution of the maximum Richardson increment (Eq. (5.12)) during the Richardson process together with the L_∞ norm of the strong residuals to the governing equations.

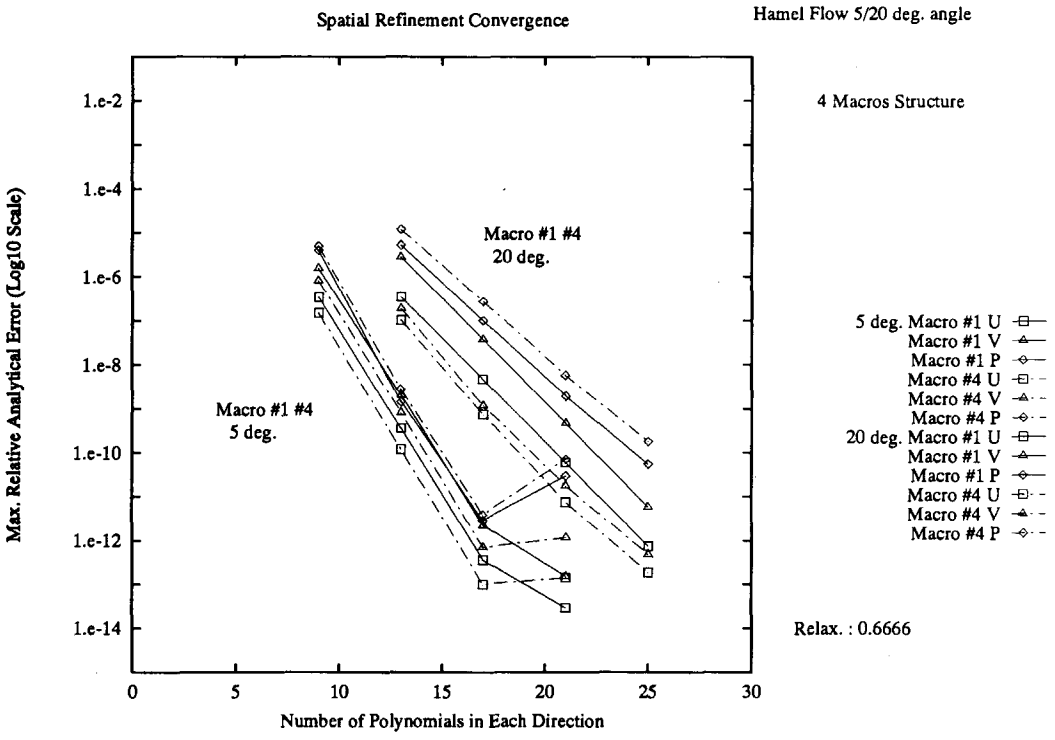

FIG. 7.5. Hamel flow in four rectilinear subdomains (5 and 20° angles): spatial refinement convergence. Evolution of the maximum relative analytical error (Eq. (7.1)) with respect to the polynomial degree in each direction.

TABLE II

Hamel Flow 5° Angle, Four Rectilinear Subdomains

d.o.f.	$\nabla_c \cdot (\mathbf{u}_{exact})$	$\nabla_c \cdot (\mathbf{u}_{comp})$
9 × 9 eq.		
Macro 1	3.7696e − 07	4.5954e − 06
Macro 2	4.1369e − 07	4.8163e − 06
Macro 3	2.8712e − 07	3.3196e − 06
Macro 4	3.1291e − 07	3.5846e − 06
13 × 13 eq.		
Macro 1	1.8119e − 09	4.5157e − 09
Macro 2	2.2397e − 09	4.9513e − 09
Macro 3	1.0645e − 09	3.0948e − 09
Macro 4	1.2981e − 09	3.3492e − 09
29 × 29 eq.		
Macro 1	1.5884e − 12	1.2285e − 12
Macro 2	1.7486e − 12	9.0245e − 13
Macro 3	1.2306e − 12	7.5294e − 13
Macro 4	1.0526e − 12	5.3957e − 12

Note. L_∞ norms of collocation divergence operator ($\nabla_c \cdot$) applied to the exact ($\mathbf{u}_{exact}$) and the computed ($\mathbf{u}_{comp}$) velocity fields for different numbers of global d.o.f.

tions in the Richardson process produce machine accuracy. For this latter case, Fig. 7.4 illustrates the evolution of the equation residuals, together with the Richardson increments produced in the process. The solution at first iteration represents a finite element solution over the Chebyshev mesh. The improvement brought to the standard FE technique by the present spectral method is quantified by several orders of magnitude gained in the accuracy after relatively few iterations. The relaxation factor was set to $\frac{2}{3}$, the value which showed the best convergence rate, independently of the geometric distortion considered.

7.1.2. *Effect of the domain decomposition.* The domain is now decomposed into four rectilinear subdomains (Fig. 7.1). Spatial refinement influence is studied in the same way as in the single-domain case for the 5 and 20° angle geometry. Similar error decay behaviour, as with a single macro structure, may be observed in this multi-domain case on Fig. 7.5: the larger the distortion, the slower the decay of the relative errors. But, at equivalent geometry and equivalent global number of d.o.f., the multi-domain solution at convergence is less accurate than the single-domain solution, as one could compare from Figs. 7.2 and 7.5. This was already referenced by Canuto [4] and Demaret [10]; geometry splitting does not affect the global number of polynomials required to seize up the solution variations. For instance, to achieve an overall 10^{-9} relative error (20° aperture), it requires 13 × 13 d.o.f. over a single domain and 17 × 17 eq. (9 × 9 over each macro) in the four-macro structure. We should emphasize that it is only true when the solution is smooth over the entire computational domain. In fact, multi-domain decomposition enhances final accuracy when it allows one to cover steep gradient regions by subdomains (in the case of boundary and/or inner layers) and therefore produces better local approximation [11].

Although the same discretization is used over the four macro elements, the quality of the polynomial representation varies as illustrated by the dispersion of the curves in Fig. 7.5. Different solution behaviours and somewhat different geometric deformations over the subdomains result in the peculiar relative accuracy level achieved. Overall error decay with refined spatial discretization is not affected. Tables II and IV present the effects of the polynomial degree and multi-domain decomposition on the accuracy. Here again, the domain decomposition does not affect the quality of the approximation: the projected computed divergence is close to the projected analytical one and drops to machine round-off. Convergence histories of the Richardson process do not depart from the single macro case: instead of a single curve for the relative error over a given variable, one finds a set of four slightly shifted curves depending on the corresponding macro but with the same trends and characteristics as in the single macro case. The relaxation factor was also set to $\frac{2}{3}$ from numerical observations.

TABLE III

Hamel Flow 20° Angle, Single Domain

d.o.f.	$\nabla_c \cdot (\mathbf{u}_{exact})$	$\nabla_c \cdot (\mathbf{u}_{comp})$
5 × 5	4.5278e − 03	5.8545e − 03
9 × 9	7.9938e − 06	1.2815e − 05
13 × 13	4.9892e − 10	8.8628e − 10

Note. L_∞ norms of collocation divergence operator ($\nabla_c \cdot$) applied to the exact ($\mathbf{u}_{exact}$) and the computed ($\mathbf{u}_{comp}$) velocity field for different numbers of global d.o.f.

TABLE IV

Hamel Flow 20° Angle, Four Rectilinear Subdomains

d.o.f.	$\nabla_c \cdot (\mathbf{u}_{exact})$	$\nabla_c \cdot (\mathbf{u}_{comp})$
13 × 13 eq.		
Macro 1	6.4986e − 06	9.0890e − 06
Macro 2	9.9423e − 06	1.3260e − 05
Macro 3	4.7190e − 07	1.7112e − 06
Macro 4	8.6107e − 07	2.5386e − 06
25 × 25 eq.		
Macro 1	2.1004e − 11	3.2658e − 11
Macro 2	2.9127e − 11	4.3611e − 11
Macro 3	1.4782e − 13	2.7660e − 12
Macro 4	1.9725e − 13	8.0460e − 12

Note. L_∞ norms of collocation divergence operator ($\nabla_c \cdot$) applied to the exact ($\mathbf{u}_{exact}$) and the computed ($\mathbf{u}_{comp}$) velocity field for different numbers of global d.o.f.

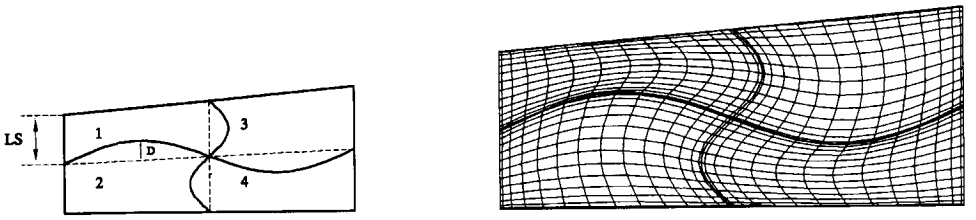

Bulging Decomposition 29x29 d.o.f. eq.

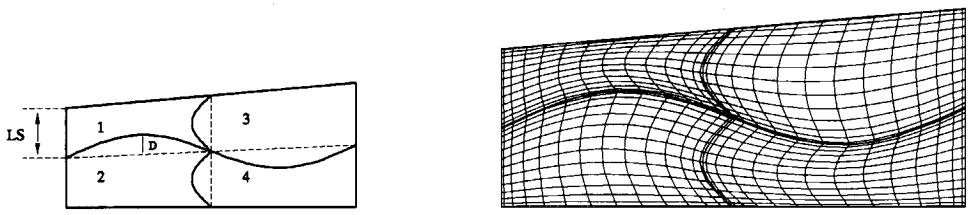

Wedging Decomposition 29x29 d.o.f. eq.

FIG. 7.6. Hamel flow at 5° angle: sketches of the curvilinear domain decomposition in "wedging" and "bulging" cases and the corresponding meshes for a 29 × 29 eq. d.o.f. over the entire geometry. LS denotes the typical length scale of the decomposition.

7.1.3. *Effect of the curvilinear distortion.* To treat large grid distortions, the geometry of the divergent channel at a 5° aperture is decomposed into four curved macro elements. The effect of increasing deformation is studied. The subdomain curvature is obtained by the superposition of a sine wave over the separating segments between the subdomains. The curvilinear distortion parameter D is defined as the ratio of the sine wave amplitude to a macro characteristic length. Two types of decomposed geometry are considered: the first decomposition (referred to as "wedging") creates a sharp wedge in the subdomains geometry, the second one does not (called "bulging"). Typical meshes are shown in Fig. 7.6. On Figs. 7.7, one can note that even for a small value of the distortion parameter D the loss in accuracy is quantified by several orders of magnitude, whether wedges are present or not in the geometry. The polynomial representation must be increased to 15 × 15 polynomials in each macro element (29 × 29 global degrees of freedom) to reach machine round-off in the least distorted cases. This striking feature of the distortion effect is enlightened by comparison of L_∞ norm values of the collocation divergence operator in Tables II, V, and VI when the global d.o.f. are equivalent. For the 13 × 13 case, we observe a loss of about five orders of magnitude (40% distortion with respect to the rectilinear case). We interpret this loss by the high-degree polynomial representation of F

TABLE V

Hamel Flow 5° Angle, Four Curved Macro Elements 40% Distortion, "Wedging" Configuration

d.o.f.	$\nabla_c \cdot (\mathbf{u}_{exact})$	$\nabla_c \cdot (\mathbf{u}_{comp})$
13 × 13 eq.		
Macro 1	3.5078e − 03	2.0810e − 03
Macro 2	9.3185e − 04	9.6124e − 04
Macro 3	1.1274e − 03	1.2314e − 03
Macro 4	1.1275e − 03	5.8347e − 04
29 × 29 eq.		
Macro 1	1.2176e − 09	1.0321e − 08
Macro 2	2.8921e − 09	2.3490e − 09
Macro 3	1.4689e − 09	2.7792e − 08
Macro 4	7.6778e − 10	1.9147e − 09

Note. L_∞ norms of collocation divergence operator ($\nabla_c \cdot$) applied to the exact velocity field ($\mathbf{u}_{exact}$) and the computed one ($\mathbf{u}_{comp}$) for different numbers of global d.o.f.

TABLE VI

Hamel Flow 5° Angle, Four Curved Macro Elements 40% Distortion, "Bulging" Configuration

d.o.f.	$\nabla_c \cdot (\mathbf{u}_{exact})$	$\nabla_c \cdot (\mathbf{u}_{comp})$
13 × 13 eq.		
Macro 1	9.7599e − 04	8.2640e − 04
Macro 2	9.3183e − 04	8.2640e − 04
Macro 3	1.1275e − 03	7.5131e − 04
Macro 4	1.1275e − 03	5.3394e − 04
29 × 29 eq.		
Macro 1	2.7310e − 09	1.9941e − 09
Macro 2	2.8921e − 09	2.1137e − 09
Macro 3	7.7462e − 10	8.8139e − 10
Macro 4	7.6775e − 10	8.6647e − 10

Note. L_∞ norms of collocation divergence operator ($\nabla_c \cdot$) applied to the exact velocity field ($\mathbf{u}_{exact}$) and the computed one ($\mathbf{u}_{comp}$) for different numbers of global d.o.f.

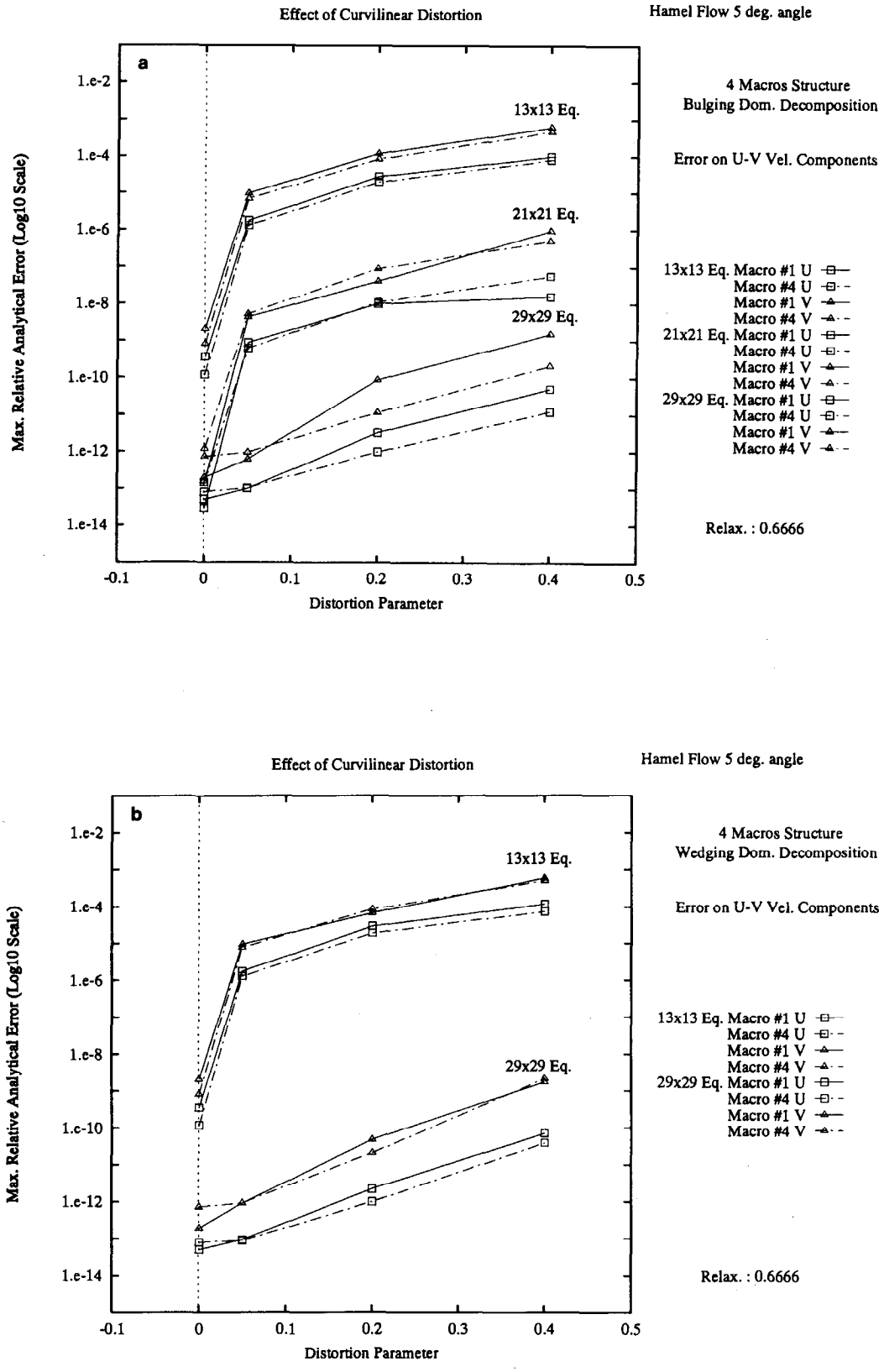

FIG. 7.7. Hamel flow in four curved subdomains 5° angle; bulging (a) and wedging (b) cases: effect of the curvilinear distortion. Evolution of the maximum relative analytical error (Eq. (7.1)) with respect to the distortion parameter for different spatial discretizations.

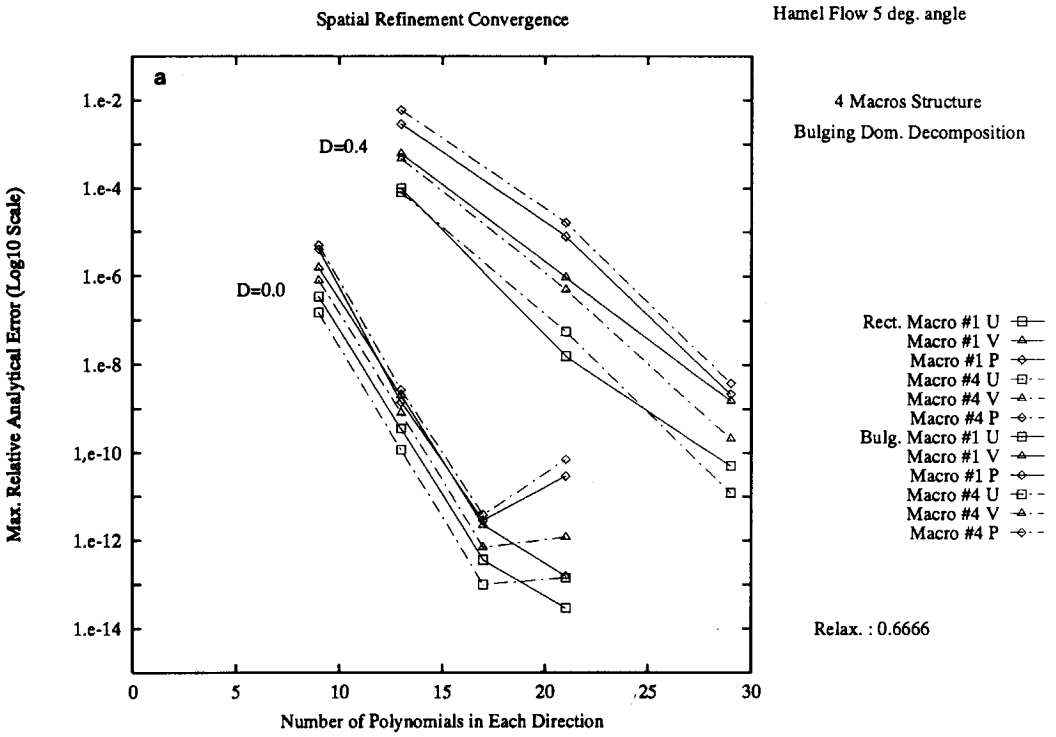

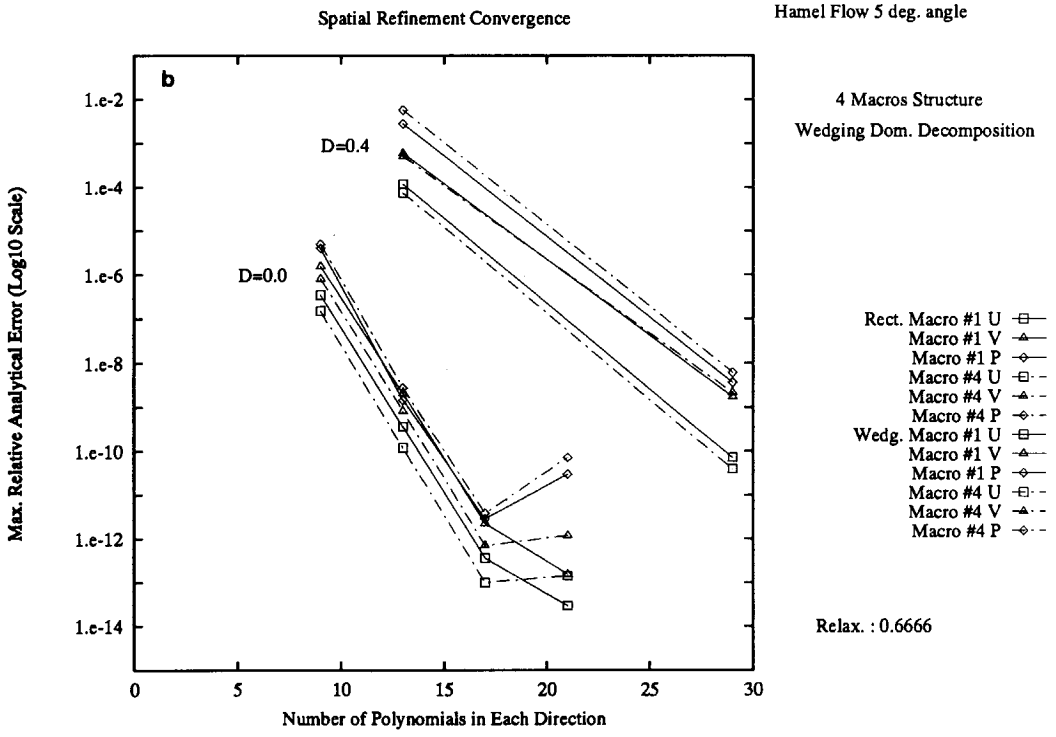

FIG. 7.8. Hamel flow in four curved subdomains 5° angle; bulging (a) and wedging (b) case: spatial refinement convergence. Evolution of the maximum relative analytical error with respect to the polynomial degree in each direction.

which induces non-constant coefficients in all derivatives. Therefore, an accurate approximation of the divergence operator requires almost a doubled polynomial degree in order to resolve both the velocity field and the mapping complexity. Even for low distortion, the presence of the trigonometric functions in the mapping has a large impact on the final accuracy (Fig. 7.7). But still, the mesh refinement effect exhibits in both cases a spectral convergence as demonstrated by Figs. 7.8. It is noteworthy that the very distorted elements in the "wedging" case do not alter the solution compared to the "bulging" case (same levels of relative errors and projected divergence). Typical velocity and pressure plots are shown in Fig. 7.9a–c for the most distorted cases to illustrate the overall C^1 continuity achieved by the method.

7.2. *Wannier–Stokes Flow*

As a second test problem, we consider the two-dimensional steady Stokes flow past a cylinder close to a moving wall. The computational domain is open except for the bottom wall which moves in its own plane with constant velocity. The analytical solution, derived from Wannier [31] in the theory of lubrication for this complex-geometry flow allows also for reliable study of the errors induced by non-rectangular geometries in the present solution procedure. Other authors also solved this problem as a test case [24]. The exact solution and the particular parameters of the test are given by

$$
\begin{aligned}
u = &-\frac{2(A+Fy)}{K_1}\left\{(s+y)+\frac{K_1}{K_2}(s-y)\right\}-F\ln\left(\frac{K_1}{K_2}\right)\\
&-\frac{B}{K_1}\left\{(s+2y)-\frac{2y(s+y)^2}{K_2}\right\}\\
&-\frac{C}{K_2}\left\{(s-2y)-\frac{2y(s-y)^2}{K_2}\right\}-D;\\
v = &-\frac{2x(A+Fy)}{K_1K_2}(K_2-K_1)-\frac{2Bxy(s+y)}{K_1^2}\\
&-\frac{2Cxy(s-y)}{K_2^2};
\end{aligned}
\tag{7.3}
$$

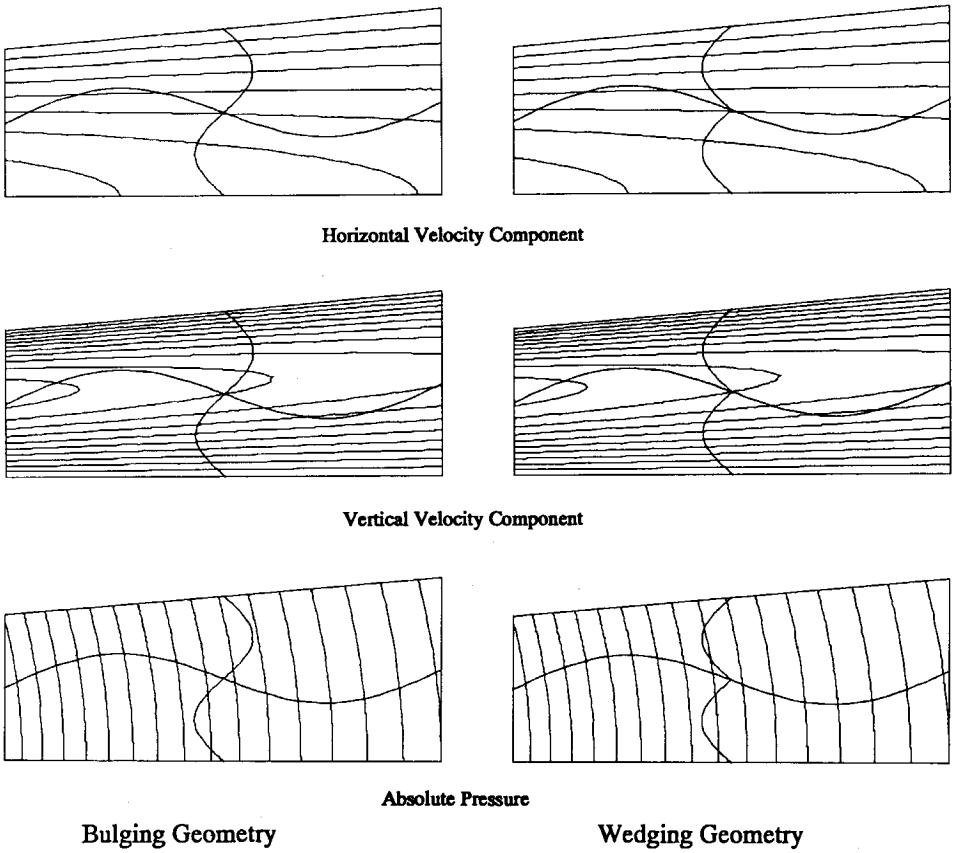

FIG. 7.9. Hamel flow in four curved subdomains 5° angle: isocontour lines of (a) the horizontal velocity component; (b) the vertical velocity component; (c) the absolute pressure; in the "wedging" (left) and "bulging" (right) cases.

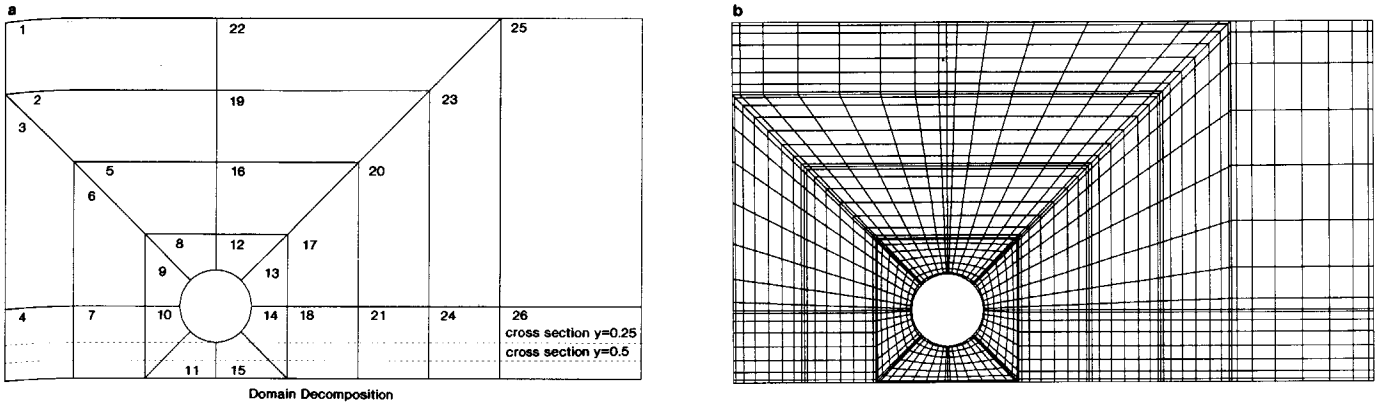

FIG. 7.10. Wannier–Stokes flow: sketch of the curvilinear domain decomposition (a) and the corresponding mesh with 9×9 d.o.f. per subdomain (b).

with

$$A = -\frac{U_w d}{\ln(\Gamma)}; \qquad B = \frac{2U_w(d+s)}{\ln(\Gamma)},$$

$$C = \frac{2U_w(d-s)}{\ln(\Gamma)}, \qquad D = -U_w,$$

$$F = \frac{U_w}{\ln(\Gamma)}, \qquad \Gamma = \frac{(d+s)}{(d-s)};$$

$$K_1 = x^2 + (s+y)^2, \qquad K_2 = x^2 + (s-y)^2,$$

$$s^2 = d^2 - R^2.$$

The length scale (LS) is four times the radius R of the cylinder, the distance d from the cylinder center to the wall is 0.5, and the constant wall velocity U_w is 1.

To solve this Stokes problem, the geometry was decomposed into 26 subdomains. The spatial discretizations varied from 5×5, 9×9, and to 11×11 d.o.f. in both directions for each subdomain. The structure and a typical mesh are shown in Figs. 7.10. The essential boundary conditions used at the boundaries of the truncated domain were computed from the exact solution (7.3). Computed velocity components, vorticity, and pressure fields (obtained with the 9×9 discretization) are displayed in Figs. 7.11a–d. The effect of the refined spatial discretization is illustrated in Fig. 7.12 for typical subdomains in the geometry. The decay of the relative analytical error is also exponential but very distorted curvilinear macro elements limit its rate over the entire geometry. This is also illustrated in Table VII, where we compare the L_∞ norms (over the collocation nodes) of the collocation divergence operator $\nabla_c \cdot$ applied on the exact and on the converged velocity field as well. The effect of the high distortion is found in the relatively slowest decay in the most distorted macro element (macro #11) and in the largest L_∞ norm. One should note that this macro also covers the region between the cylinder and the moving wall where the flow exhibits its full dynamics. Although the accuracy achieved in the coarsest mesh is poor, that mesh still provides a good approximation of the solution as demonstrated in Fig. 7.13 by the pressure profiles computed at different horizontal cross sections in the geometry (refer to Fig. 7.10 a for the definition of these cross sections).

TABLE VII

Wannier–Stokes Flow

d.o.f.	$\nabla_c \cdot (\mathbf{u}_{\text{exact}})$	$\nabla_c \cdot (\mathbf{u}_{\text{comp}})$
Macro 11		
5×5	4.66746e − 01	4.36279e − 01
9×9	8.51745e − 03	8.05868e − 03
11×11	8.71785e − 04	8.27297e − 04
Macro 23		
5×5	7.17430e − 04	7.76506e − 04
9×9	3.55075e − 08	7.14591e − 07
11×11	4.86738e − 10	1.08367e − 08

Note. L_∞ norms of collocation divergence operator ($\nabla_c \cdot$) applied to the exact velocity field ($\mathbf{u}_{\text{exact}}$, as in Eqs. (7.3)) and the computed one ($\mathbf{u}_{\text{comp}}$) for different numbers of global d.o.f.

In this last problem, we consider a plane channel presenting a cosine constriction (Fig. 7.14). This problem was already treated by finite element methods [7] and fourth-order compact differences [2]. The channel presents a longitudinal symmetry and the computational domain is thus restricted to its upper half. The geometry is divided into

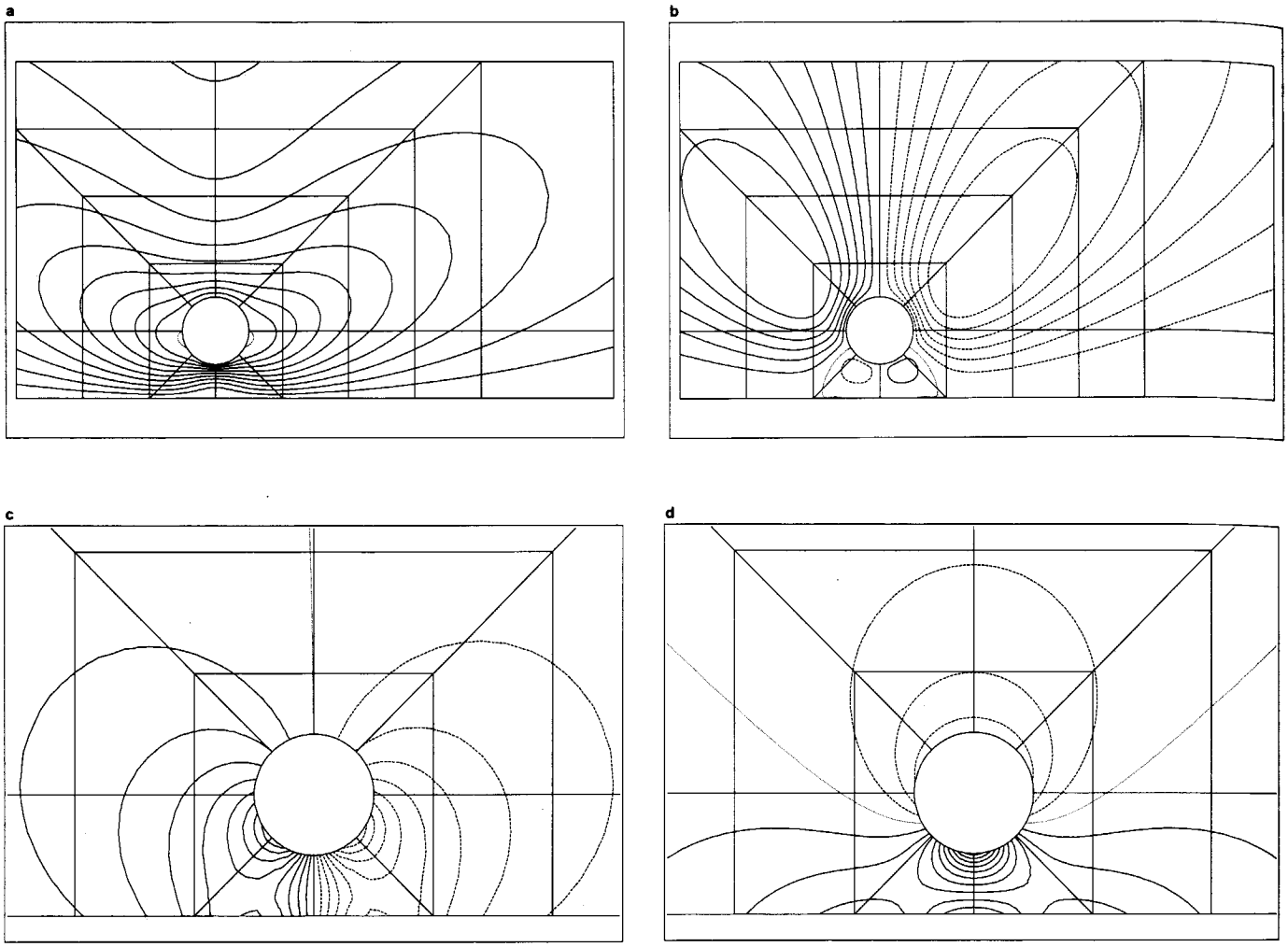

FIG. 7.11. Wannier–Stokes flow: isocontour lines of (a) the horizontal velocity component (global view); (b) the vertical velocity component (global view); (c) the absolute pressure (enlarged view around the cylinder); (d) the vorticity (enlarged view around the cylinder).

three parts whose respective lengths are l_1, 1, and l_2. Each boundary section is described by the functions:

$$y(x) = \pm 1; \qquad 0 \leqslant x \leqslant l_1$$

$$= \pm 1 \pm \frac{\lambda}{2}(1 - \cos 2\pi(x - l_1)); \qquad l_1 \leqslant x \leqslant l_1 + 1$$

$$= \pm 1, \qquad l_1 + 1 \leqslant x \leqslant l_1 + l_2 + 1,$$

where λ is the constriction parameter whose values range between zero and one. This parameter compares a channel typical length scale LS (the channel half-width) and the depth of the cosine constriction. The Reynolds number is defined as the ratio of the total flow rate per unit length and the kinematic viscosity. The total flow rate per unit length was set to two and the inflow and outflow boundary conditions are:

(i) at the inlet, a Poiseuille velocity profile: $u = 1.5(1 - y^2)$, $v = 0$;

(ii) at the outlet, natural boundary conditions: $t_n = 0$, $v = 0$;

(iii) on the symmetry axis: $\partial u/\partial n = 0$, $v = 0$;

with t_n the normal component of the stress vector (Eq. (2.4)).

The lengths l_1 and l_2 are chosen long enough such as to ensure a reasonable development of the flow far away of the constriction. The upstream region l_1 is 3.5 long and the downstream region length l_2 is 9.5. In this paper the only results presented are obtained for the 50% constriction, which exhibits a strong geometric stiffness. The computa-

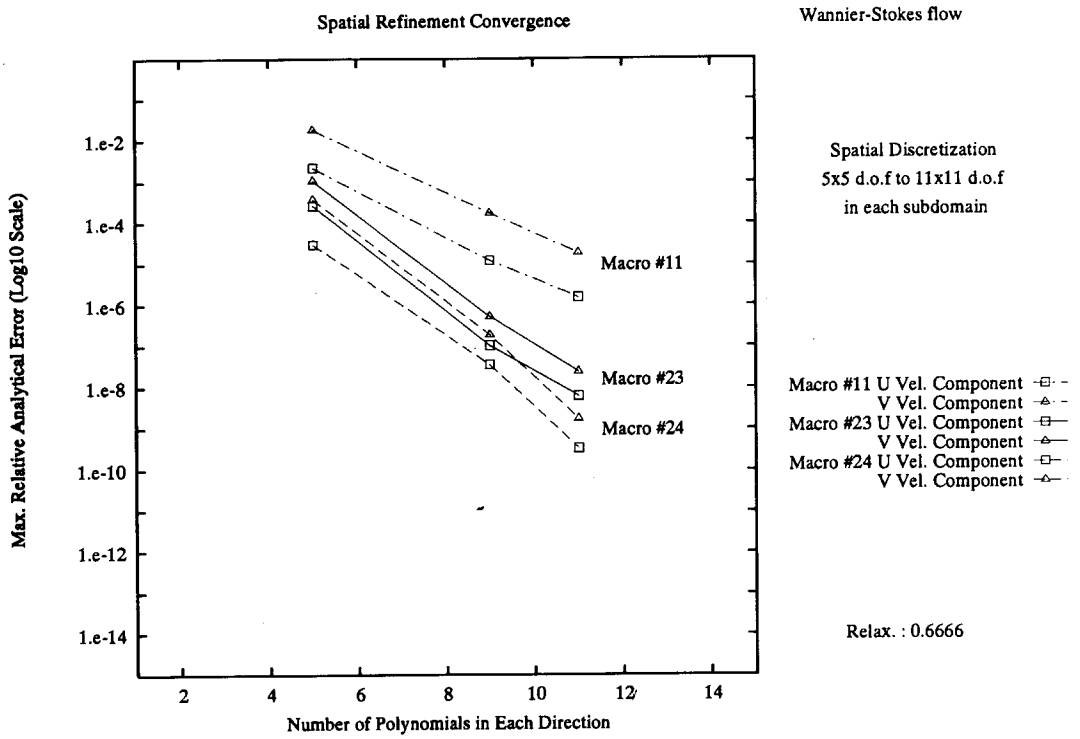

FIG. 7.12. Wannier–Stokes flow: spatial refinement convergence. Evolution of the maximum relative analytical error with respect to the polynomial degree in each direction for some typical subdomains (refer to Fig. 7.10a).

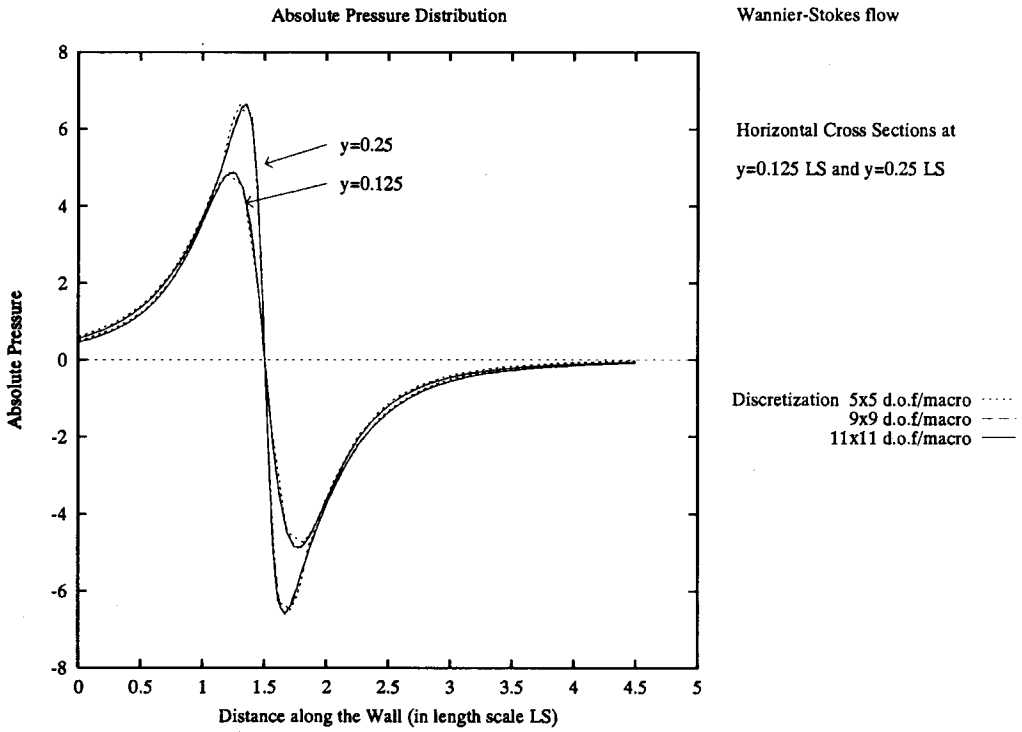

FIG. 7.13. Wannier–Stokes flow: evolution of the absolute pressure along chosen horizontal cross sections under the cylinder (refer also to Fig. 7.10a) for different polynomial degrees.

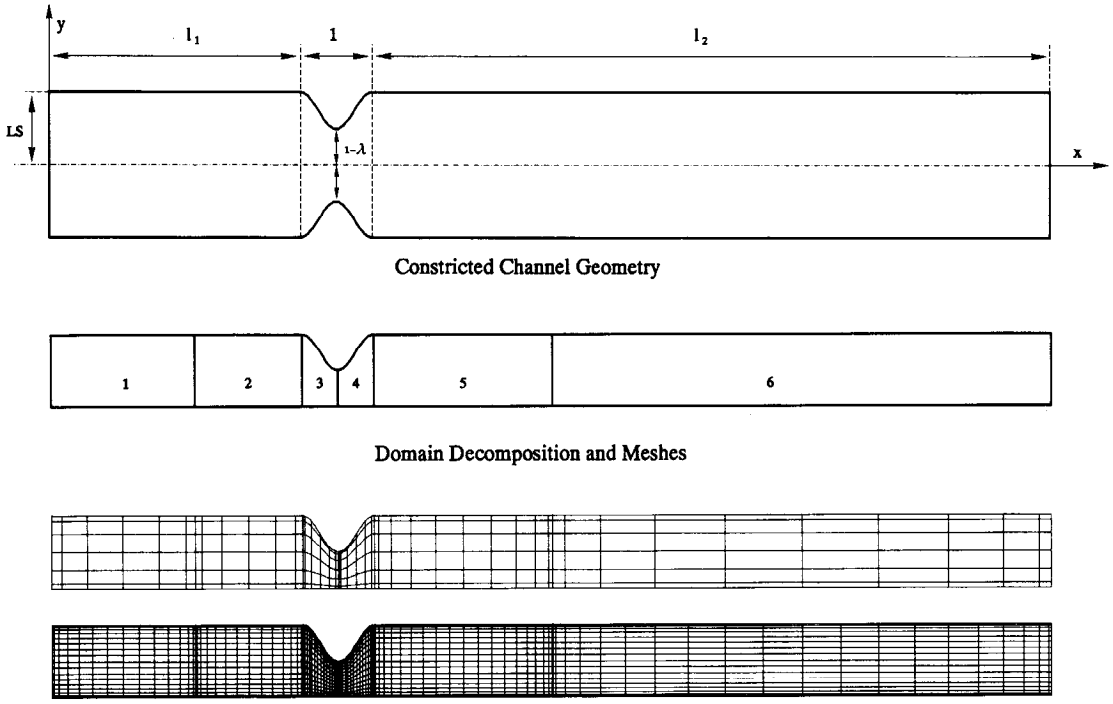

FIG. 7.14. Plane constricted channel: (a) definition of the problem geometry; (b) sketch of corresponding domain decomposition; (c) $D1$ discretization mesh; (d) $D4$ discretization mesh.

tional domain was split into six subdomains with four different spatial discretizations "Di's" (the discretization must conform at subdomain interfaces) which are characterized by the number of polynomials used in the two macro elements under the constriction, $D1: 7 \times 7$; $D2: 11 \times 11$; $D3: 15 \times 15$; and $D4: 19 \times 19$.

The channel flow was simulated at increasing Reynolds numbers 0, 50, and 100. The Figs. 7.15a–d detail the solution obtained at $\mathrm{Re} = 100$ over the $D3$ discretization in the form of velocity components, pressure, and vorticity contours, with the focus on the constriction region. The reader should note the apparent C^1 continuity at the macro interfaces of the vorticity field, which, as a secondary variable spectrally computed from the velocity components representation, is not ensured to be C^1 by the method. Table VIII illustrates the spatial refinement effect in this case by means of the

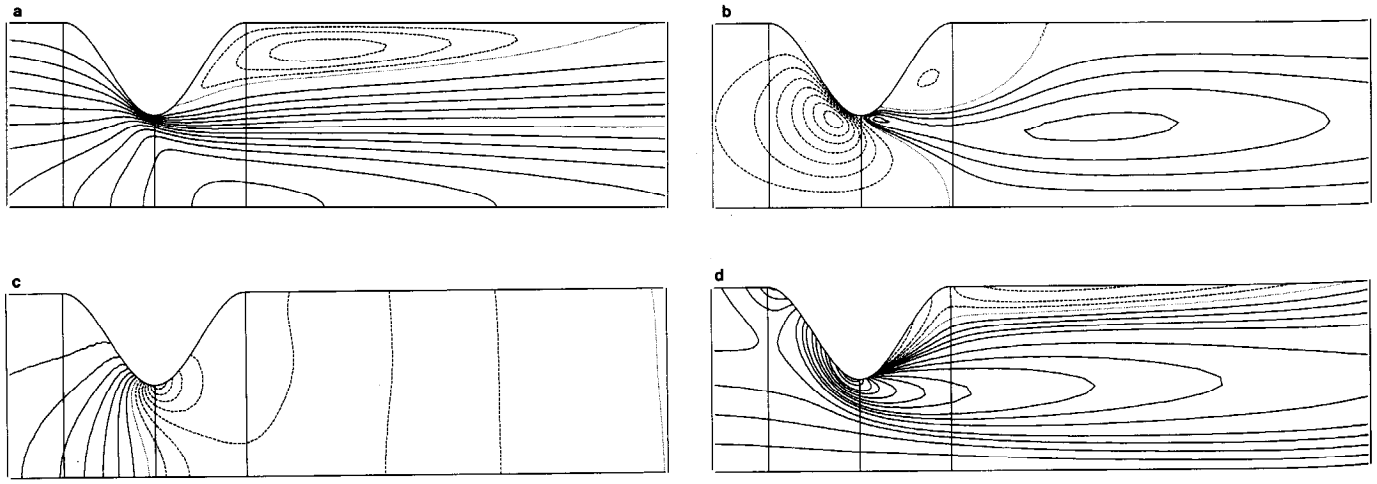

FIG. 7.15. Plane constricted channel (50% constriction) at Re 100: isocontour lines of (a) the horizontal velocity component (enlarged view around the neck); (b) the vertical velocity component (enlarged view around the neck); (c) the absolute pressure (enlarged view around the neck); (d) the vorticity (enlarged view around the neck).

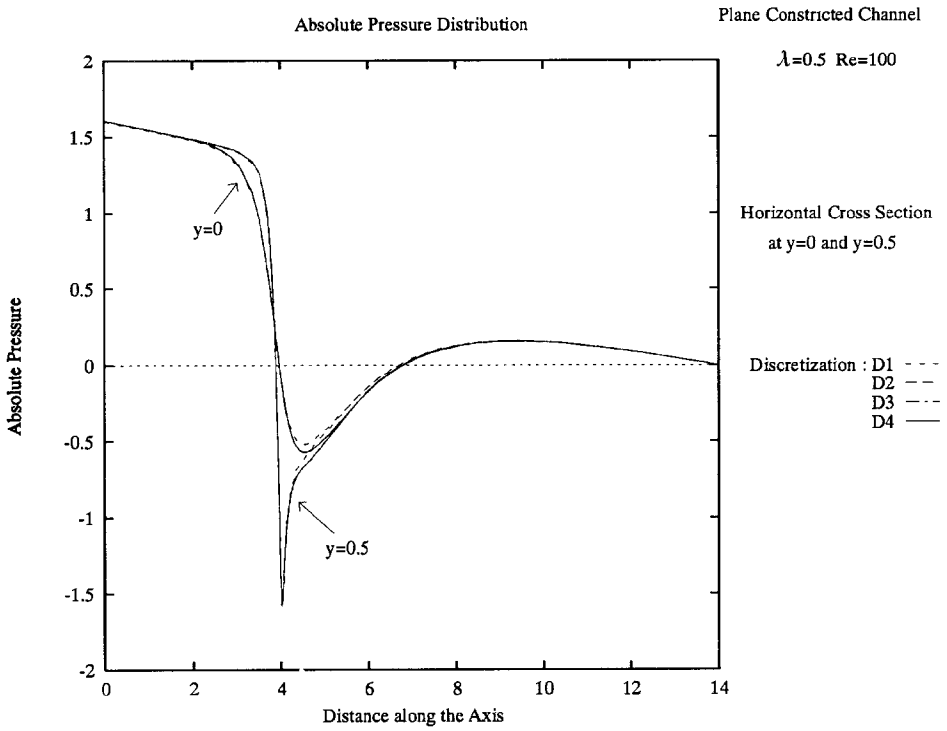

FIG. 7.16. Plane constricted channel (50% constriction) at Re 100: evolution of the absolute pressure along longitudinal cross sections in the channel ($y=0$ symmetry axis and $y=0.5$ just under the neck).

variation of the L_2 norm of the velocity field divergence with the increasing polynomial degree in the strongly distorted macro elements on the constriction at the convergence of the Newton process. For the finest discretization used, the L_2 norm rates about 10^{-2} after five Newton iterations while the last Newton corrections go down to 10^{-11} for the velocity components and 10^{-9} for the pressure. The same effect is checked in Fig. 7.16 and Fig. 7.17 by the compared evolution of some chosen variables with larger and larger polynomial degree. But for the coarsest $D1$ discretization, all the evolution curves obtained cannot be distinguished, demonstrating that the solution is spatially converged. The $D2$ discretization provided satisfactory results although on plots similar to those of Fig. 7.15 some wiggles are present in the contour lines. The strong constriction (50% over one scale length) generates noteworthy steep gradients around the neck: in the vertical velocity component (Fig. 7.15), in the absolute pressure (Fig. 7.16), or in the stress components (Figs. 7.17) (the wall shear stress is normalized by the corresponding Poiseuille wall shear stress). Those gradients explain the relatively high value in the residuals obtained, even for the most refined mesh. Such steep variations do not alter the performances of a spectral method if they coincide with one subdomain interface. Unfortunately, this is not the case in this problem as the wall shear peak is located slightly upstream of the contraction neck. But the quality of the results in such problems proves the robustness of the method.

TABLE VIII

Constricted Channel Flow, 50% Constriction at Re = 100

7×7	9.245e−02	1.657e−01
11×11	5.527e−03	1.411e−02
15×15	2.433e−04	5.432e−03
19×19	5.599e−05	1.797e−04

Note. Discrete L_2 norms of continuity equation residual (at convergence after five Newton iterations) for different numbers of d.o.f. in the third and fourth macro elements (see Fig. 7.14).

8. CONCLUSIONS

We are able to solve the steady Navier–Stokes equations in complex curved geometries with the proposed Chebyshev collocation method. The latter is preconditioned by a finite element technique based on biquadratic velocities and bilinear pressures. Relative errors in model curvilinear

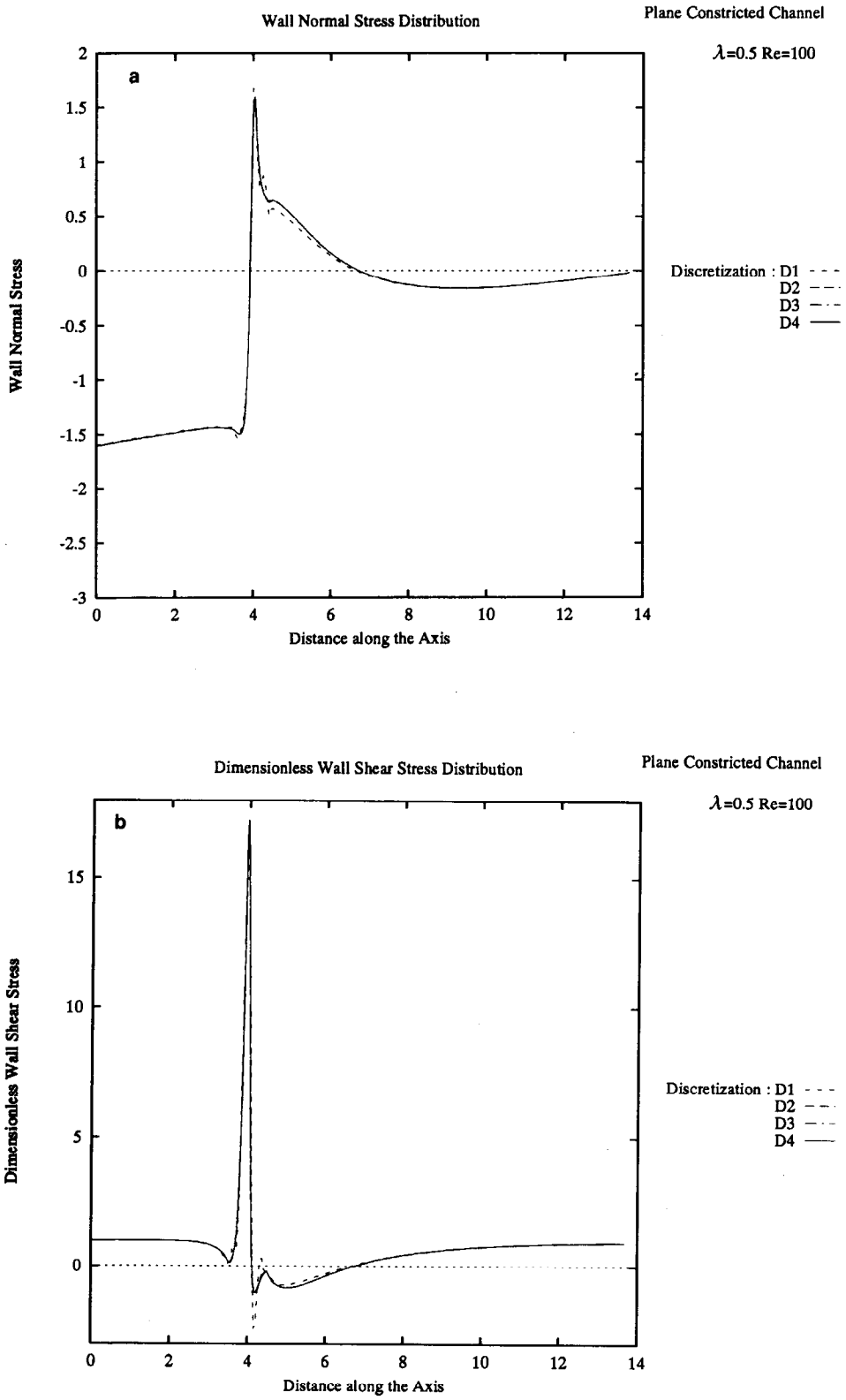

FIG. 7.17. Plane constricted channel (50% constriction) at Re 100: (a) evolution of the wall normal stress; (b) evolution of the normalized wall shear stress.

Stokes problems present exponential decay whether the geometry is decomposed into subdomains or not. This demonstrates that the outstanding convergence properties provided by the Chebyshev polynomials still hold even in non-rectangular geometries. Complicated Navier–Stokes flows in a constricted channel were simulated using our multi-domain algorithm.

The extension of our coupled velocity–pressure method to 3D problems is not immediate. The coexistence of both spectral and FE inf–sup compatible discretizations would limit drastically the applicability of the method to large size problems in terms of incore memory. The obvious aim is to reduce the number of unknowns required for the FE part of the algorithm. To this end, the mini element introduced by Arnold, Brezzi, and Fortin [1] based upon $Q1$ velocities and $Q1$ pressure approximations, including a bubble function is certainly a good candidate. In order to reduce the size of the algebraic systems to solve, a fully decomposed procedure could also be designed to solve iteratively each local subproblem.

REFERENCES

1. D. A. Arnold, F. Brezzi, and M. Fortin, *Calcolo* **21**, 337 (1984).
2. X. Aubert and M. Deville, *J. Comput. Phys.* **49**, 490 (1983).
3. C. Canuto, M. Y. Hussaini, A. Quarteroni, and T. A. Zang, *Spectral Methods in Fluid Dynamics* (Springer-Verlag, New York, 1988).
4. C. Canuto and P. Pietra, *J. Comput. Phys.* **91**, 310 (1990).
5. T. F. Chan, R. Glowinski, J. Periaux, and O. B. Widlund, in *Proceedings, Second International Symposium on Domain Decomposition Methods, Los Angeles, California, January 14–16* (SIAM, Philadelphia, 1988).
6. T. F. Chan, R. Glowinski, J. Periaux, and O. B. Widlund, in *Proceedings, Third International Symposium on Domain Decomposition Methods for Partial Differential Equations, Houston, Texas, March 20–22* (SIAM, Philadelphia, 1989).
7. R. T. Cheng, *Phys. Fluids* **15**, 2098 (1972).
8. P. Ciarlet, *The Finite Element Method for Elliptic Problems* (North-Holland, Amsterdam, 1978).
9. P. Demaret and M. O. Deville, *J. Comput. Phys.* **83**, 463 (1989).
10. P. Demaret and M. O. Deville, *J. Comput. Phys.* **95**, 359 (1991).
11. P. Demaret, M. O. Deville, and C. Schneidesch, *Appl. Numer. Math.* **6**, 107 (1989/1990).
12. M. O. Deville, "Chebyshev Collocation Solutions of Flow Problems," Spectral and High Order Methods for Partial Differential Equations, Proceedings, ICOSAHOM'89, Italy, 1989, p. 27.
13. M. O. Deville and G. Labrosse, *J. Comput. Appl. Math.* **8**, 293 (1982).
14. M. O. Deville and E. H. Mund, *J. Comput. Phys.* **60**, 517 (1985).
15. M. O. Deville and E. H. Mund, *SIAM J. Sci. Stat. Comput.* **12**, 311 (1990).
16. M. O. Deville and E. H. Mund, *SIAM J. Sci. Stat. Comput.* **13**, 596 (1992).
17. P. R. Eisemann and G. Erlebacher, *Grid Generation for the Solution of Partial Differential Equations*, NASA CR-178365, Icase Report no. 85-57, 1987 (unpublished).
18. A. Farcy and T. Alziary de Roquefort, *Comput. and Fluids* **16**, 459 (1988).
19. A. George and J. W. Liu, *SIAM J. Numer. Anal.* **17**, 282 (1980).
20. W. J. Gordon and C. A. Hall, *Numer. Math.* **21**, 109 (1973).
21. W. J. Gordon and C. A. Hall, *Geometric Aspects of the Finite Element Method with Application to Partial Differential Equations*, edited by A. K. Aziz (Academic Press, New York/London, 1972), p. 769.
22. P. Haldenwang, G. Labrosse, S. Abboudi, and M. Deville, *J. Comput. Phys.* **55**, 115 (1984).
23. G. Hamel, *Jahresber. Deutsch. Math. Verein.* **25**, 34 (1916).
24. G. E. Karniadakis, M. Israeli, and S. A. Orszag, *J. Comput. Phys.* **97** (2), 414 (1991).
25. D. A. Korczak and A. T. Patera, *J. Comput. Phys.* **62**, 361 (1986).
26. Y. Maday and A. T. Patera, "Spectral Element Methods for the Incompressible Navier–Stokes Equations," State-of-the-Art Surveys on Computational Mechanics, edited by A. K. Noor and J. T. Oden (ASME, New York, 1989), p. 71.
27. B. Metivet, Thèse de doctorat d'état, Université Pierre et Marie Curie, Paris 6, 1987 (unpublished).
28. M. E. Mortenson, *Geometric Modeling* (Wiley, New York, 1985).
29. S. A. Orszag, *J. Comput. Phys.* **37**, 70 (1980).
30. C. R. Schneidesch, Doctorat en Sciences Appliquées, Université Catholique de Louvain, Louvain-la-Neuve, 1992 (unpublished).
31. G. H. Wannier, *Q. Appl. Math.* **8**, 1 (1950).